

Contents lists available at ScienceDirect

Acta Materialia

journal homepage: www.elsevier.com/locate/actamat





Selective oxidation and nickel enrichment hinders the repassivation kinetics of multi-principal element alloy surfaces

Jia Chen ^a, Zhengyu Zhang ^a, Eitan Hershkovitz ^e, Jonathan Poplawsky ^b, Raja Shekar Bhupal Dandu ^a, Chang-Yu Hung ^a, Wenbo Wang ^a, Yi Yao ^c, Lin Li ^{c,*}, Hongliang Xin ^d, Honggyu Kim ^{e,*}, Wenjun Cai ^{a,*}

- a Department of Materials Science and Engineering, Virginia Polytechnic Institute and State University, VA 24061, United States
- ^b Center for Nanophase Materials Sciences, Oak Ridge National Laboratory, TN 37831, United States
- ^c School for Engineering of Matter, Transport and Energy, Arizona State University, Tempe, AZ 85287, United States
- ^d Department of Chemical Engineering, Virginia Polytechnic Institute and State University, VA 24061, United States
- ^e Department of Materials Science and Engineering, University of Florida, Gainesville, FL 32603, United States

ARTICLE INFO

Keywords: Multi-principal element alloys High entropy alloys Corrosion Tribocorrosion Repassivation

ABSTRACT

Robust and sustained corrosion resistance in multi-principal element alloys (MPEA) requires rapid repassivation, i.e. regrowth of the passive layer once it is damaged or destroyed at the surface. In this study, we show that the repassivation of Al_{0.1}CrCoFeNi MPEA in 0.6 M NaCl solution is hindered at pH of \sim 2.4 - 6.8 due to the formation of a Ni-enriched subsurface layer as a result of selective oxidation and dissolution of several principal elements, which can be fully restored at pH of \sim 14 from the oxidation of all principal elements. Specifically, surface characterization via X-ray photoelectron spectroscopy (XPS), high-angle annular dark-field (HAADF) imaging in scanning transmission electron microscopy (STEM), and atom probe tomography (APT), are coupled with density functional theory (DFT) calculations to determine surface composition, oxidation state, and electron work function to uncover the structural origin of the pH-dependent repassivation mechanisms. It was found that selective oxidation of Cr, Co, and Fe in the acidic to neutral solutions altered the surface composition to be significantly enriched in Ni as compared to the bulk. Once the original passive film is destroyed locally by either pitting or tribocorrosion, this altered surface composition exhibited a much poorer repassivation capability due to the increased electron work function and reduced surface reactivity at higher Ni concentration. These understandings could shed light on the future compositional design of non-equiatomic MPEAs towards sustained repassivation and corrosion resistance over a wide pH range.

1. Introduction

Multi-principal element alloys (MPEAs), also known as high entropy alloys (HEAs), and complex concentrated alloys (CCAs), are an emerging class of metallic materials often consisting of four or more alloying elements with similar atomic concentrations [1–7]. MPEAs possess several unique properties that set them apart from conventional alloys. These include superior fatigue [8–10] and wear resistance [11–13], high strength and toughness at extremely low and high temperatures [14], and excellent corrosion resistance [15–18]. Many MPEAs exhibit excellent aqueous corrosion resistance due to the formation of a single phase solid solution [19], hence eliminating micro-galvanic coupling in traditional engineering alloys such as aluminum alloys [20], magnesium

alloys [21], and stainless steel [22], where the different partitioning of alloying elements in alloy matrix vs. precipitates and secondary phases often leads to different surface Volta potentials between the constituent phases, and eventually preferential corrosion of the more anodic phases of the alloy. For example, several MPEAs such as single phase face-centered-cubic FeCrCoNi [19] and eutectic FeCrNiCoNb_{0.5} [23] and AlCoCrFeNi_{2.1} [24] are reported to exhibit better corrosion resistance than 304 stainless steel in chloride containing environments solutions. Several recent reviews [25,26] summarize the corrosion behavior and mechanisms of MPEAs in great breadth and depth. It is also worth pointing out that while a lot of past effort has focused on optimizing individual material properties (e.g. corrosion resistance) of MPEAs, our recent DFT study [27] shows that simultaneously optimizing both

E-mail addresses: lin.li.10@asu.edu (L. Li), honggyukim@ufl.edu (H. Kim), caiw@vt.edu (W. Cai).

^{*} Corresponding authors.

mechanical and corrosion properties requires the relaxation of the equi-atomic composition, where the non-equiatomic compositions (e.g. $Cr_{34}Co_{22}Fe_{22}Ni_{22}$) exhibit a better combination of mechanical and corrosion properties than its equiatomic counterpart.

J. Chen et al.

So far, most studies have been focused on the corrosion resistance and passivation ability of MPEAs [28,29], yet little is known about their repassivation ability [30]. In corrosive environments, passive metals resist corrosion by forming a very thin (typically a few nanometers thick), oxidized, and protective passive film on their surfaces to significantly reduce metal dissolution beneath the film. Should such passive film be damaged or destroyed mechanically, such as during stress corrosion cracking (SCC) [31] and tribocorrosion [32-36], a rapid repassivation of the de-passivated regions (e.g. the newly fractured or scratched surface) often takes place in oxygen containing environment (e.g. air, naturally aerated water) to restore the lost passivity. This oxidation process has been explained by a Cabrera-Mott model via a high electric field growth mechanism by some researchers [37,38], who suggest that the high electric field in the oxide leads to the migration of both cation and anion, resulting in the surface oxidation. Alternatively, others [39,40] show that a low-field point defect model best explains the oxidation process where oxygen diffuses towards the oxide/metal interface via exchanging positions with vacancies in the oxides. Nonetheless, the kinetics of repassivation, where the damaged passive film reforms via oxidation, is widely recognized as a crucial factor in determining an alloy's susceptibility to SCC and tribocorrosion [31,41,42]. For SCC, according to the slip dissolution model [43], the crack initiation and propagation proceeds via the rupture of the passive film followed by repetitive dissolution and repassivation events on the crack surfaces [44,45]. The repassivation kinetics has often been studied via the place exchange model [44,45] from rapid scratch electrode experiments [41,44,45] as well as via the critical repassivation temperature from potentiodynamic polarizations experiments [46]. For tribocorrosion, our previous tribocorrosion studies revealed that passive alloys such as Al-alloys and steel readily repassivate in a few seconds after wear [32–36,47,48], while active alloys such as Mg alloys remain in an active corrosion mode during and after the wear test [49,50]. These results indicate that it is important to have an adequate concentration of passive elements (e.g. Al, Ti, and Cr) to obtain excellent repassivation capability. Ayyagari et al. [51] investigated the tribocorrosion behaviors of Al_{0.1}CoCrFeNi and CoCrFeMnNi MPEAs in dry and marine environment, concluding that the passive film of Al_{0.1}CoCrFeNi with higher Cr content was more stable than that of CoCrFeMnNi. Nair et al. [52] reported an exceptionally high tribocorrosion resistance of Al_{0.1}CoCrFeNi compared to SS316L steel, which was related to the formation of a stable passive layer on the MPEA.

The inherent repassivation rate of MPEAs depends upon various environmental and material properties such as the solution pH, temperature, and the alloy composition, especially the concentration of passive elements [31,44,46]. In terms of the effects of passive element such as Cr, a recent study by Gerard et al. [28] showed that $\text{Ni}_{38}\text{Fe}_{20}\text{Cr}_x\text{Mn}_{21\text{-}0.5x}\text{Co}_{21\text{-}0.5x}$ with less than \sim 10 at. % Cr was marginally passive or active while those with ≥ 10 at. % Cr exhibited well defined passive behavior in 1 mM NaCl solution at pH=4. Furthermore, it was shown that corroded surface composition is rather complex, with an inner layer (i.e. the altered zone) that is depleted in Cr yet enriched in Ni, and an outmost passive layer enriched with Ni and Cr, while other principal elements such as Fe, Mn, and Co showed congruent dissolution. Thus, a better understanding of the repassivation kinetics of MPEAs requires a systematic study that links surface and subsurface compositions to the repassivation kinetics. Understanding the repassivation ability of MPEAs under simultaneous stress and corrosion is critical for designing high performance alloys under extreme environmental conditions. The goal of this work is to understand the repassivation ability of MPEAs as a function of pH, and identify the structural origin necessary for sustained passivity under surface stress to enable future alloy design for extreme environments. Motivated by previous reports [51,52], a

single phase MPEA alloy Al_{0.1}CrCoFeNi was chosen for this study, which exhibit more stable passive film compared to CoCrFeMnNi and higher tribocorrosion resistance than that of SS316L due to the addition of \sim 2.45 at.% Al. Note that if much higher concentration of Al is added to CrCoFeNi MPEA, the corrosion resistance is often deteriorated. For example, Kuwabara et al. [53] investigated the corrosion behavior of equiatomic AlCoCrFeNi with ~ 20 at.% Al in 3.5 wt.% NaCl aqueous solution. Such high Al concentration leads to the formation of multiple phases, including FCC, B2 and BCC phases, and resulted in slightly worse corrosion resistance than SUS304 stainless steel. The electrolyte after corrosion was found to contain high levels of Al and Ni ions due to their dissolution, while Cr forms stable oxide films on the metal surface. In other words, in AlCoCrFeNi alloys with relatively high Al concentration, the addition of Al not only promotes multiphase formation, which often results in micro-galvanic corrosion among various constituting phases, but also is largely absent in surface oxidation. A similar trend was observed by Kao et al. [54], who found that the increased Al concentration in $Al_xCoCrFeNi$ (x = 0, 0.25, 0.50, 1.00) alloys resulted in a more porous surface film and poorer corrosion resistance.

In this work, repassivation behavior of a single phase $Al_{0.1}$ CrCoFeNi MPEA was studied in NaCl aqueous solutions. Solution pH was varied from 2.4 to 14, allowing the study of the passivation behavior (as well as the lack of it) of MPEA from acidic to basic conditions. Understanding the pH effects is important for potential applications of MPEAs in chemical treatment, food and drug production industries, nuclear power plant and marine engineering, etc. [51,55,56]. The specific goals of this work include 1) determining the effects of pH on the repassivation ability of $Al_{0.1}$ CrCoFeNi MPEA after simultaneous wear and corrosion, 2) characterizing the surface composition, electronic states, and atomic structure of corroded and tribocorroded MPEA, and 3) identifying the structural origin responsible for sustained repassivation capability of MPEA under different pH values by linking experimental observations with thermodynamic predictions and DFT calculations.

2. Materials and methods

2.1. Materials, corrosion, and tribocorrosion testing

Al $_{0.1}$ CrCoFeNi alloys were received from Sophisticated Alloys, Inc. (Pennsylvania, USA), with the following nominal composition (at.%): 2.1% Al, 24.5% Cr, 24.7% Co, 24.5% Fe and 24.2% Ni. The alloy was manufactured via vacuum induction melting and cast into a $2.5\times2.5\times9$ inch 3 ingot, followed by hot isostatic pressing at 2,200 °F, 15 ksi for 4 h. Prior to testing, all samples were ground by silica sandpapers with gritnumbers of 180, 240, 400, 600 and 1200, polished by alumina polishing suspension (particle size of 1 μ m, 0.3 μ m, and 0.05 μ m), and finally rinsed with ethanol and dried in air.

Corrosion tests of the alloys were performed using a potentiostat/ galvanostat/zero resistance ammeter (Gamry model 600, Pennsylvania, USA) with a three-electrode setup at 25 \pm 2 °C. The sample, a mixed metal oxide coated titanium mesh, and silver-silver chloride (Ag/AgCl) electrode were used as the working (WE), counter (CE), and reference electrode (RE) with 1 M KCl internal solution, respectively for all electrochemical measurements. All samples were covered by protective lacquer with a 1 cm² exposed area prior to the tests. The samples were tested via cyclic potentiodynamic (CPD) and potentiostatic polarization in 0.6 M NaCl solution with various pH values (pH = 2.43, 6.41 and 13.95), adjusted by adding small amounts of HCl or NaOH in solution, representing an acidic, neutral, and basic solution. After stabilizing at open circuit potential (E_{ocp}) for 30 mins, CPD curves were recorded with a scan rate of 0.167 mV/s for 1 h. The stabilization time of 30 min was chosen as the corrosion potential remains relatively stable after ~ 1200 seconds immersion, as shown in Fig. S1(a) in the supplemental materials. A potential of 200 mV below $E_{\text{\scriptsize ocp}}$ was setup as an initial potential. CPD scan was reverted at 10^{-2} A/cm². CPD scan was finished until one complete cycle was formed. The potentiostatic measurements were conducted at a constant anodic potential of 300 mV above E_{ocp} for 3,600 s. All tests were repeated three times. An example of repeated tests is given in Fig. S1(b) in the supplemental materials.

For the tribocorrosion testing, a multifunctional tribometer (Rtec MFT-5000, Rtec, California, USA) was connected to a potentiostat/gal-vanostat/zero resistance ammeter (Gamry Reference 600^{TM} system) for the tribocorrosion tests in 0.6 M NaCl solution under various pH values (same as the electrochemical tests) at $25\pm2\,^{\circ}\text{C}$. An alumina ball (4 mm diameter) was used as the counter body. Tribocorrosion tests were performing using the alloy as the WE, and the same CE and RE as the corrosion tests, as shown in Fig. 1. For each test, the sample surfaces were worn by the counter body under 5 N normal force and 1 Hz sliding frequency, over 5 mm scratch length for 300 s, at ambient temperature (25 \pm 2 C). All tribocorrosion tests were performed under E_{ocp} , which was stabilized for 2,500 s prior to each test. Once the scratching finished, the counter body was lifted up and the sample was kept in the solution for another 700 s. A new alumina ball was used for each test to minimize contamination. All tests were repeated three times.

2.2. Materials characterization

As-received, corroded and tribocorroded samples were characterized to determine their crystallographic information, composition and oxidation state. X-ray diffraction (XRD, PANalytical X'pert PRO MRD) was carried out on the as-received alloy with 2.5 s scan step time, 0.01° step size, using Cu Ka under 45 kV and 40 mA. Microstructure characterization of the as-received samples was conducted using the Thermo Scientific Helios 5 DualBeam FIB-SEM, operated with an applied voltage of 20 kV and a current of 13 nA. To acquire the electron backscatter diffraction (EBSD) patterns, EDAX APEX software was used. EBSD mapping was obtained with a step size of 6 µm, and further analysis of the data was performed using EDAX OIM software. The surface morphology and microstructure after tribocorrosion tests were analyzed by a scanning electron microscopy (SEM, Quanta 600 FEG, FEI, Oregon, USA). Energy-dispersive X-ray spectroscopy (EDS, Quantax, Bruker, Massachusetts, USA) was used to characterize the chemical composition of the worn and unworn areas after tribocorrosion test under 15 KeV. Wear track were measured by DektakXT stylus profiler (Bruker, USA). Xray photoelectron spectroscopy (XPS, PHI Quantera SXM, USA) characterization was used to investigate the chemical state within the passive film on both worn and unworn areas under an ultra-high-vacuum system (10^{-9} Torr). To minimize the native oxide film growth in air, all samples were measured in XPS immediately after exposure to the NaCl solution. The survey spectrum was obtained by a monochromatic Al $K\alpha$ X-ray source (a beam diameter of 100 μm and an angle of 45° analyzer). Carbon contamination on the surface was removed by pre-sputtering using 1 kV ion beam for 15 s. All spectrum was calibrated by C 1s at 284.8 eV. MultiPak analysis software was used to deconvolve the

spectrum after the curve fitting.

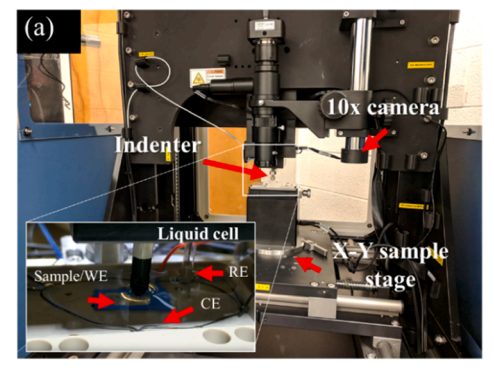
Characterization of the corroded surface was performed using atom probe tomography (APT). Prior to APT specimen preparation, the anodized samples were coated with 100 nm of Ni or Cr using a South Bay Technologies IBS/e ion beam deposition system. APT specimens were prepared using standard focused ion beam (FIB) lift out and sharpening methods using a Thermo Fisher Nova 200 dual beam SEM/FIB [57]. In summary, equilateral triangular prisms were lifted out, mounted on Si microtip array posts, sharpened using a 30 kV Ga⁺ ion beam, and cleaned using a 2 kV Ga⁺ ion beam leaving the sputtered metallic cap at the needle surface. The APT experiment was run using a CAMECA LEAP 4000XHR in laser mode with a 30K base temperature, 60-100 pJ laser power, a detection rate of 1 ion per 200 pulses, and a 200 kHz pulse repetition rate. The APT results were reconstructed and analyzed using CAMECA's interactive visualization and analysis software (IVAS 3.8).

Characterization of tribocorrosion damage and elemental distribution were carried out using scanning transmission electron microscopy (STEM) and energy-dispersive X-ray spectroscopy (EDS). Cross-section specimens for STEM and EDS studies were prepared using a Thermo Scientific Helios G4 PFIB CXE Dual Beam FIB/SEM. A final cleaning cycle of the TEM specimens was conducted using Xe ions at 2 kV. Highangle annular dark-field (HAADF) imaging in STEM was performed using a Themis Z (Thermo Fisher Scientific) equipped with a probe aberration corrector. The accelerating voltage of the microscope was 200 keV and the semi-convergence angle of the electron probe was 22 mrad. EDS elemental maps were obtained using a four-quadrant Super-X EDS detector with a 300 pA beam current and a pixel dwell time of 20 μs .

2.3. Pourbaix diagram and DFT calculations

In this study, Pourbaix diagrams of pure metal (Al, Cr, Co, Fe, Ni), binary (Cr $_{55}$ Ni $_{55}$) and ternary (Cr $_{33}$ Co $_{33}$ Fe $_{33}$, Cr $_{33}$ Co $_{33}$ Ni $_{33}$, Fe $_{33}$ Ni $_{33}$, Fe $_{33}$ Ni $_{33}$ Cr $_{33}$) alloys were calculated using Materials Project database [58–60]. Those of quaternary (CrCoFeNi) and quinary (Al $_{0.1}$ CrCoFeNi) alloys were calculated using the Thermo-Calc software (version 2023b) due to limitations of Materials Project database for calculating more than four principal elements. These calculations were performed at 25°C and 1 atm, with approximately 1 kg of water and about 1×10^{-4} mole of each metal element in the alloy. Ions present at concentrations lower than 1×10^{-9} mole were disregarded in the plotted diagrams. The database employed for the Al $_{0.1}$ CrCoFeNi composition included: PAQ2_v2.5 + ALDEMO_v4.1 + TCAQ3.1 + OXDEMO4.0. For the CrCoFeNi and Cr19Co26Fe21Ni34 compositions, the database utilized was: PAQ2_v2.5 + FEDEMO_v5.0.

Spin-polarized density functional theory (DFT) calculations were performed using the Vienna *ab initio* simulation package (VASP) [61,62] with the projected augmented plane-wave (PAW) method. Structure optimization was carried out using the Perdew-Burke-Ernzerhof (PBE)



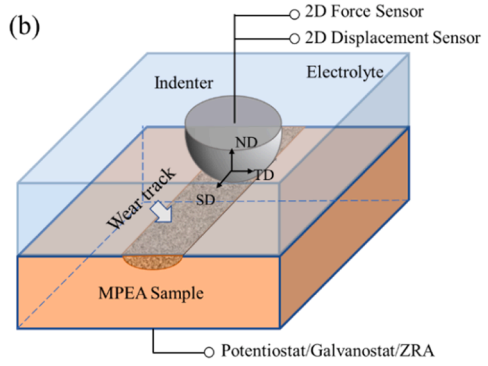


Fig. 1. (a) Photo and (b) schematic illustrations of the linear reciprocal ball-on-disc tribocorrosion testing setup. Inset in (a) shows the closed-up view of the liquid cell where WE, CE, and RE represents the working, counter, and reference electrode respectively. The coordination system is defined in (b), where SD, TD, and ND represents the scratching, transverse, and normal direction respectively.

generalized gradient approximation (GGA) exchange-correlation functional [63], with an energy cutoff 400 eV. The supercell structure was relaxed until the Hellmann-Feynman forces on each atom was less than 0.03~eV/Å and energy convergence criterion was $10^{-5}~\text{eV}.$ Special quasirandom structure (SQS) method [64] was used in this work to create periodic random alloy cells via the alloy theoretic automated toolkit (ATAT) package [65]. Lattice constant was calculated over a 128-atom cell with $(5\times5\times5)$ Monkhorst-Pack mesh of k-points. Electron work function (EWF) was calculated by a cell of 256 atoms with a $(1 \times 1 \times 1)$ k-point mesh. We also note here that the present DFT calculation was constrained by the limited number of atoms that could be processed with the available computational resources, posing challenges in accommodating the highly diluted element Al. Experimental results in Section 3 affirm that Al concentration remained below 5 at.% in both the passive layer and bulk material, notably smaller compared to Co, Cr, Fe, and Ni. Consequently, we utilized a slab without Al to simulate the effects of Co, Cr, Fe, and Ni in the DFT calculations.

3. Results

3.1. XRD characterization and repassivation behavior during corrosion

Fig. 2(a) shows the XRD plot of as-received Al $_{0.1}$ CrCoFeNi alloy, indicating the presence of a single-phase face centered cubic (fcc) structure with a strong (200) texture along the sample normal direction (ND, as defined in Fig. 1(b)). Such fcc structure is also consistent with prior reports on MPEAs with similar compositions [51,66]. It is also noted that in Al $_{\rm X}$ CrCoFeNi-based alloys, increasing the Al content was found to lead to a phase transformation from a single fcc phase at x<0.3,

to a dual phase of fcc+bcc when x \approx 0.5, and a complete bcc phase at even higher x values [67]. Fig. 2(b) shows the EBSD map of the as-received alloy, where relatively large and defect-free grains can be detected. Using a line-intercept method, the average grain size is estimated to be \sim 1.73 \pm 1.15 mm.

To determine both the pitting and repassivation behavior of this alloy at different pH, CPD tests were performed as it separates the pitting and repassivation potentials by minimizing the incubation time and maximizing pit growth right after its initiation using a reverse scan [68–70]. Fig. 2(c) shows the typical CPD curves of Al $_{0.1}$ CoCrFeNi in 0.6 M NaCl aqueous solution as a function of pH and Table 1 summarizes all measured electrochemical parameters. Under all pH conditions, passivation was dominating the anodic reactions until its breakdown at high potentials. Close to the breakdown potentials, current oscillations

Table 1 Summary of the electrochemical parameters of $Al_{0.1}$ CrCoFeNi from cyclic polarization tests at various pH values in 0.6 M NaCl solutions. E_{ocp} , E_{corr} , E_{pit} , E_{prot} represents the open circuit, corrosion, pitting, and protection potential respectively. All potentials are reported vs. the Ag/AgCl reference electrode. The passivation current I_{pass} is measured at ~ 300 mV above the E_{corr} for each pH condition.

pН	E _{ocp} (V)	E _{corr} (V)	E _{pit} (V)	E _{prot} (V)	I _{pass} (A/cm ²)
2.43	-0.10 \pm	-0.12 \pm	$1.07~\pm$	-0.05 \pm	(5.23 ± 1.72)
	0.05	0.05	0.04	0.03	$\times 10^{-6}$
6.41	-0.024 \pm	-0.079 \pm	$1.11~\pm$	$0.13~\pm$	(2.00 ± 0.21)
	0.01	0.001	0.05	0.01	$ imes 10^{-6}$
13.95	-0.35 \pm	-0.35 \pm	_	_	$(1.99\pm0.30)\times$
	0.03	0.03			10^{-5}

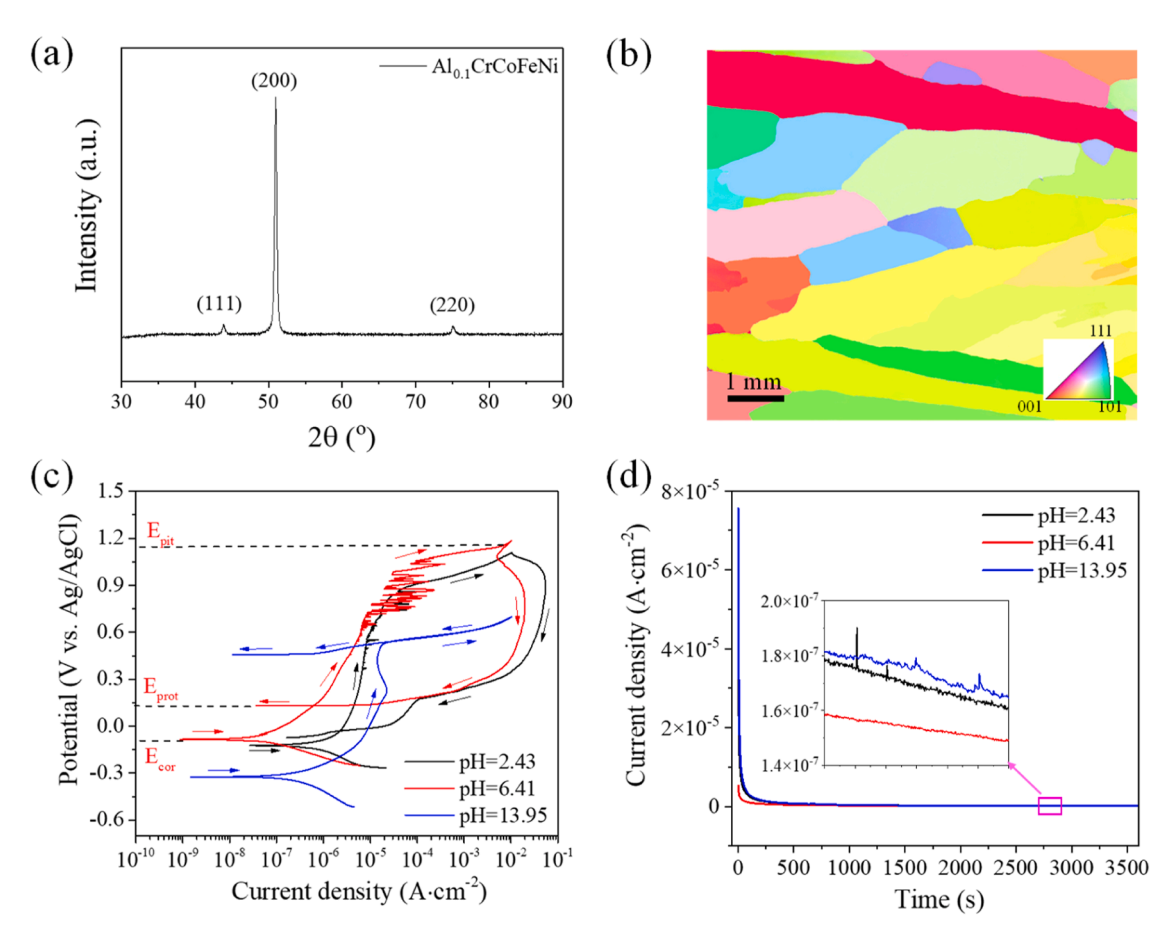


Fig. 2. (a) XRD 2θ plot and (b) EBSD map of the as-received of as-received $Al_{0.1}$ CrCoFeNi alloy, with lattice orientation in the sample normal direction (ND) color coded according to the inset legend, (c) typical cyclic polarization curves from three repeated tests, and (d) current evolution at 0.3 V anodic potential above OCP of $Al_{0.1}$ CrCoFeNi under different pH conditions.

were observed under pH of 2.43 and pH 6.41 conditions, likely due to metastable pitting behavior on the sample surface. Among all pH conditions, the highest breakdown potential of ~1.18 V vs. Ag/AgCl was observed under pH = 6.41, whose hysteresis loop area is similar to that of pH = 2.43. Under pH = 6.41, the protection potential (E_{prot}) was around 0.13 V vs. Ag/AgCl, higher than its corrosion potential (E_{cor} = -0.08 V vs. Ag/AgCl). E_{prot}, also known as the repassivation potential, corresponds to the potential at which pits repassivate on the reserve scan. Even preexisting pits will repassivate and stop growing if the potential becomes more negative than E_{prot}. Although still under active debate, it is generally believed that a more positive value of both Epit and E_{prot} corresponds to the less likelihood of pit initiation and propagation. Nonetheless, the reversed potential scan obtained under pH = 13.95shows no hysteresis loop, different from the other two pH conditions, indicate that the material was immune to pitting corrosion at the basic solution, where any pit formation can be readily repassivated. This excellent repassivation capability of Al_{0.1}CoCrFeNi in the basic, rather than the acidic to neutral solution is indeed confirmed later on using tribocorrosion tests, as detailed in the next section. Under the alkaline solution, an active-to-passive transition showed in the anodic polarization, characterized by a decrease of current density after active dissolution. It was believed that the saturated metal-electrolyte interface can be formed by metal cations or salts when a critical current density is reached during the active dissolution [71-73].

Interestingly, while the corrosion potential (E_{cor}) is similar for the acidic (pH = 2.43) to neutral (pH = 6.41) solution, it is much lower (\sim -0.3 V vs. Ag/AgCl) in the basic (pH = 13.95) solution. The decrease in corrosion potential results from both the left shift of the cathodic branch, and the right shift of the anodic branch [56,74]. In the basic solution, the metal dissolution rate (i.e. the anodic reaction) is thus expected to be slightly higher and the cathodic reaction (likely the oxygen reduction) rate to be lower than those from the acidic and neutral pH conditions (likely hydrogen generation).

To verify the observed passivity and confirm the differences in metal dissolution rate of Al_{0.1}CoCrFeNi under various pHs, potentiostatic polarization was carried out under an applied anodic potential of 300 mV above E_{ocp}. Fig. 2(d) shows that under all pH values studied, the current densities dropped quickly after the first ~ 200 sec and remained at extremely low values (~ 1.6 -1.8 \times 10^{-7} A/cm2) for the remaining of the test, indicating the rapid formation of a protective passive film, further supporting the CPD results. In addition, closer observation of the stabilized current densities (inset in Fig. 2(d)) indicated that the current densities are slightly higher at higher pH values, in agreement with the

CPD results discussed earlier. Additional surface SEM characterization (see in the supplemental materials) confirms that micrometer-sized pits formed in the acidic to neutral solutions, while no detectable pits is observed in the basic solution.

The corrosion studies show that a passive film can quickly form on the surface of $Al_{0.1}$ CoCrFeNi at all pH values, yet local breakdown (in the forms of pit formation) of the passive film can only be readily repaired at pH = 13.95, but not pH = 2.43 and 6.41, suggesting a much better repassivation capability of the metal surface at the basic condition. Next, we show that a Ni-rich layer developed the metal/passive layer interface at the acidic to neutral conditions, but not at the basic conditions. The formation of this layer not only affects repassivation during corrosion, but also impedes repassivation during tribocorrosion when the original passive layer is removed mechanically.

3.2. Surface characterization of passive layer via APT

To better understand the structural origin of the different corrosion behavior, the passive film composition of the anodized samples (i.e. those tested in Fig. 2(c)) were characterized by APT, as shown in Figs. 3-5. A sputtered Cr cap was used for samples tested in a pH of 2.43 and 13.95, and a Ni cap was used for samples tested in a pH of 6.41. Different caps were used to eliminate the effects of capping material on the results as both Cr and Ni are principal elements of the MPEA. In either case, the Cr/Ni cap and Ga damaged regions were removed from the APT data using concentration thresholds of each element before performing the proximity histograms using a 10 at. % O isoconcentration surface. The element concentration profile in Fig. 3 shows that at pH = 2.43, Co and Fe were largely depleted in the passive layer, and a Ni-rich subsurface layer (green shaded area) exists between the metal substrate and the outmost passive layer. In addition to the Ni enrichment, a slight depletion of Cr is also observed, where the Cr concentration drops to ~ 20 at.% from the bulk composition. This is indeed similar to the 'altered zone' observed by Gerard et al. [28] in NiFeCrMnCo MPEA after corrosion at pH of 4. The maximum Ni composition in the Ni-rich layer is ~ 32.8 at.%, significantly higher than that from the bulk concentration (~ 24.8 at.%). Towards the outmost surface of the passive layer, the Ni concentration returns to its nominal bulk concentration (~ 24.7 at.%), while the concentration of Cr, Fe, and Co is 22.0 at.%, 11.2 at.%, and 13.6 at.% respectively. A similar behavior is also observed for the sample anodized in a pH = 6.41 solution, as shown in Fig. 4, although both the Ni-rich layer and the passive film are thinner than that of the more acidic condition. The outmost

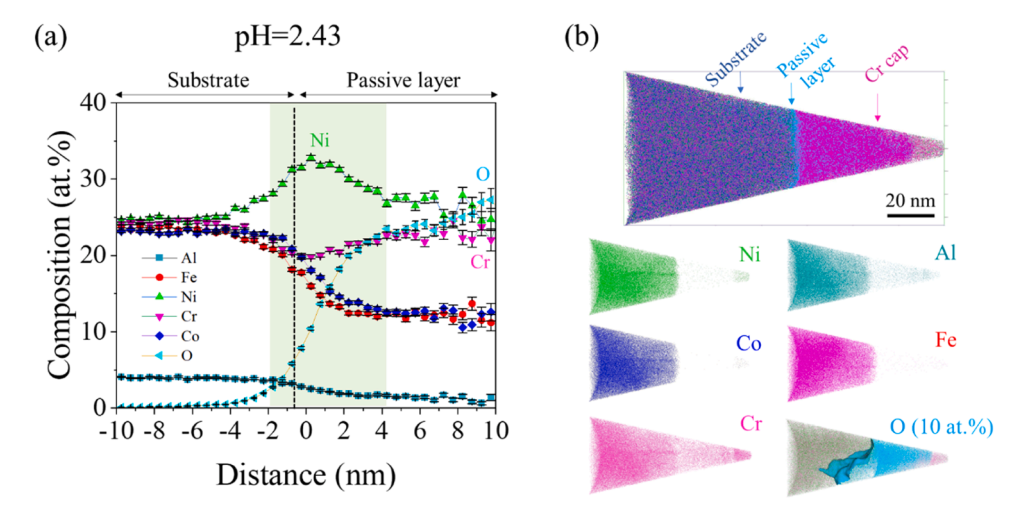


Fig. 3. (a) Proximity histogram of a 10 at.% O isoconcentration surface with the Cr cap removed. (b) APT atom maps of $Al_{0.1}$ CrCoFeNi after a 3600 s, 300 mV anodization under pH = 2.43, where a 10 at.% O isoconcentration surface with oxide ions is displayed as light blue dots and the metal ions displayed as dark blue (Co), dark pink (Fe), light pink (Cr), and green (Ni) dots. (For interpretation of the references to colour in this figure legend, the reader is referred to the web version of this article.)

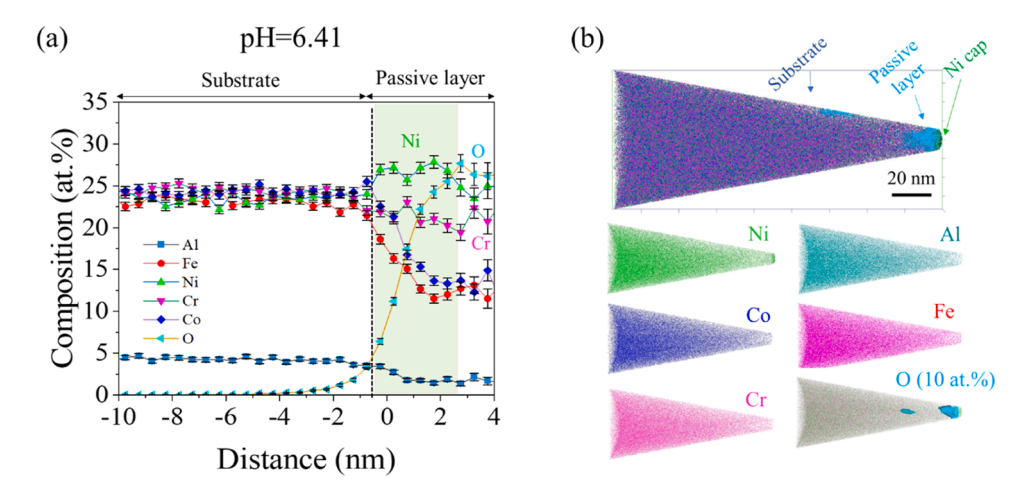


Fig. 4. (a) Proximity histogram of a 10 at.% O isoconcentration surface with the Ni cap removed. (b) APT atom maps of $Al_{0.1}$ CrCoFeNi after a 3600 s, 300 mV anodization under pH = 6.41, where a 10 at.% O isoconcentration surface with oxide ions is displayed as light blue dots and the metal ions displayed as dark blue (Co), dark pink (Fe), light pink (Cr), and green (Ni) dots. (For interpretation of the references to colour in this figure legend, the reader is referred to the web version of this article.)

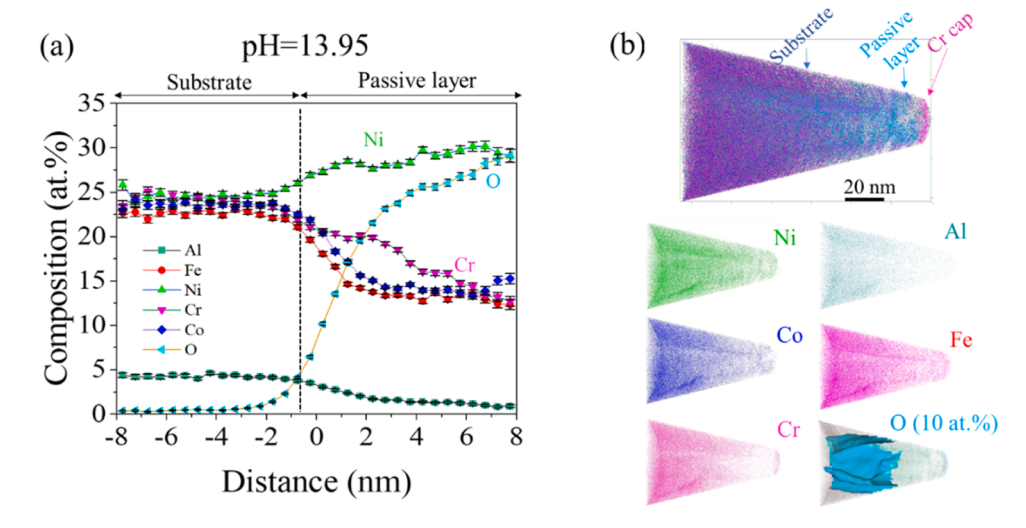


Fig. 5. (a) Proximity histogram of a 10 at.% O isoconcentration surface with the Cr cap removed. (b) APT atom maps of $Al_{0.1}$ CrCoFeNi after a 3600 s, 300 mV anodization under pH = 13.95, where a 10 at.% O isoconcentration surface with oxide ions is displayed as light blue dots and the metal ions displayed as dark blue (Co), dark pink (Fe), light pink (Cr), and green (Ni) dots. (For interpretation of the references to colour in this figure legend, the reader is referred to the web version of this article.)

surface of the passive layer has a composition of 25.0 at.% Ni, 20.7 at.% Cr, 11.5 at.% Fe, and 14.9 at.% Co. Fig. 5 shows that the elemental distribution is quite different when the sample is anodized in a pH = 13.95 solution, where all principal elements except Ni, i.e. Cr, Fe, Co, were depleted. The Ni concentration remains relatively uniform, \sim 28 – 30 at.% in the passive layer, with no clear trend of declining towards the outmost surface. The concentration of Cr, Fe, and Co is 12.7 at.%, 12.7 at.%, and 15.3 at.% respectively in the outmost passive layer.

3.3. Repassivation behavior during tribocorrosion

Fig. 6 summarizes the results of the tribocorrosion tests. Fig. 6(a) shows the evolution of open circuit potential (OCP) during the tribocorrosion test in 0.6 M NaCl solution at different pH, where the black arrows marked the start and finish of scratching wear. Before scratching, the corrosion potential remained close to a constant value of -0.06 V and -0.025 V vs. Ag/AgCl under pH = 2.43 and 6.41 respectively, higher than that (\sim -0.35 V vs. Ag/AgCl) under pH = 13.95, in agreement with the CPD results. Once scratching started, a sharp decrease of potential

occurred under all pH conditions, indicating the partial or complete removal of the passive film on the surface due to mechanical wear [33]. Due to such mechanically induced depassivation on the wear track, a micro-galvanic coupling is expected to form between the worn (local anode) and unworn (local cathode) areas, further accelerating corrosion on the worn region [75]. The corrosion potential dropped during wear was slightly greater (~ 0.35 V) at pH = 13.95 than that at pH = 2.43 (\sim 0.24 V) and pH = 6.41 (\sim 0.28 V). Once the load was removed, the corrosion potential shifted back to more positive values as a consequence of repassivation on the wear track. While the potential completely restored its initial value prior to the wear test under the basic condition (pH=13.95), it did not reach its original values in acidic (pH = 2.43) and neutral (pH = 6.41) conditions after 700 s. Once the original passive layer was mechanically removed due to wear, this Ni-rich subsurface cannot be passivated to the same level as the original MPEA, resulting in a lower corrosion potential.

To verify whether this impeded repassivation is affected by the scratching time, the OCP evolution was monitored at pH=6.41 with scratching time from 1, 5, to 10 min. Fig. 6(d) shows that the

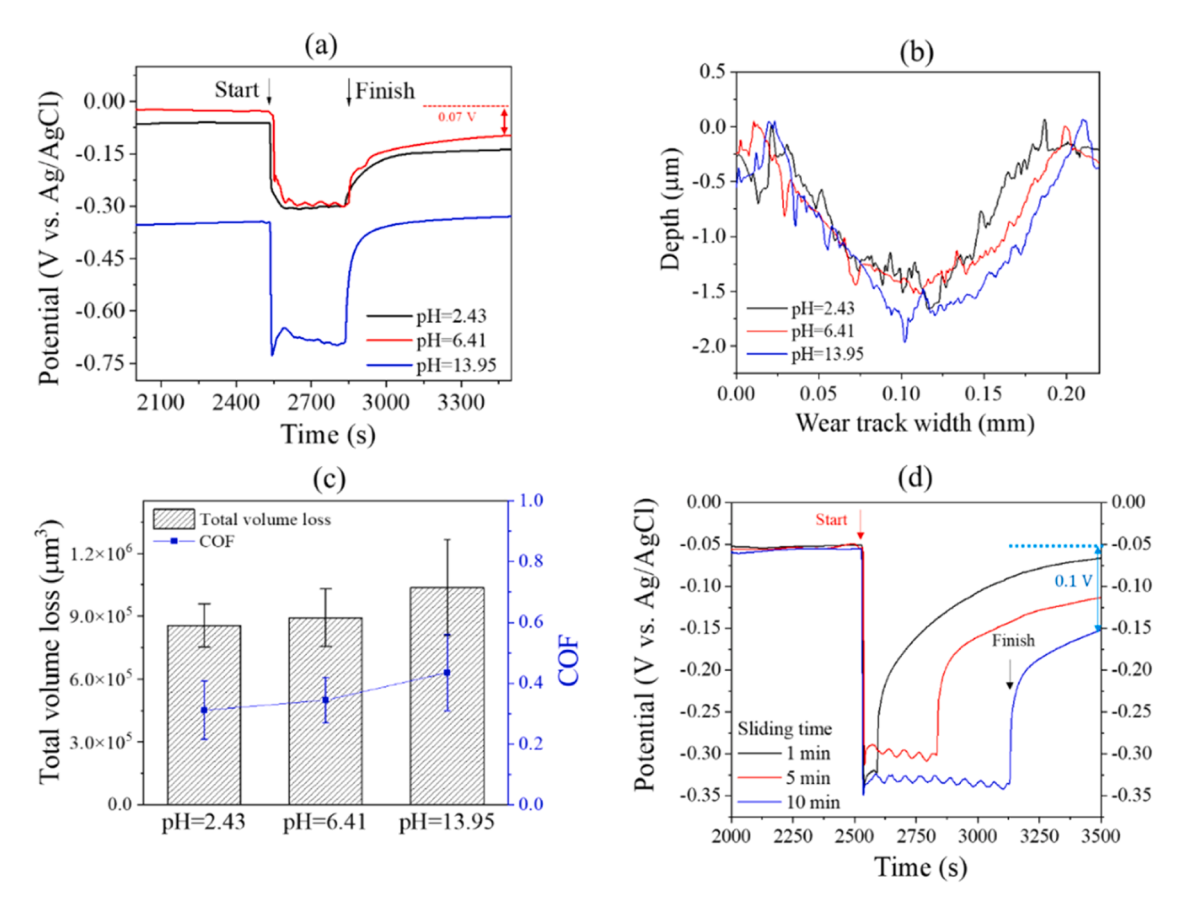


Fig. 6. (a) Evolution of open circuit potentials (OCP), (b) wear track depth profiles, and (c) total volume loss and coefficient of friction (COF) of $Al_{0.1}$ CrCoFeNi during tribocorrosion process in 3.5 wt.% NaCl aqueous solution at different pH values. and (d) evolution of OCP of $Al_{0.1}$ CrCoFeNi alloy during tribocorrosion in 3.5 wt.% NaCl aqueous solution at pH = 6.41 with different sliding time.

repassivation capability under neutral pH further decreased with increasing sliding time (e.g. ~ 0.02 V drop after 1 min sliding to ~ 0.1 V potential drop after 10 min sliding). It suggests that the formation of the Ni-rich layer at acidic to neutral solutions can impede surface repassivation (i.e. passive film self-healing), and the effect is more severe with prolonged scratching time, where the original passive film was mechanically removed. The time-dependent voltage change could be modeled using an appropriate equivalent circuit such as Randle's circuit that includes voltage-dependent circuit elements like the Tafel element and the Mott-Schottky element [76]. This is left for future work due to the lack of accurate oxide film properties such as intrinsic and extrinsic oxide resistance and capacitance at this point.

Fig. 6(b) shows the wear depth profile under the three different pH conditions. Based on the worn profile measurement, the total volume loss was calculated by multiplying the cross-sectional area of the wear track by the wear track length, as summarized in Fig. 6(c). The total material loss increased from $8.55\times10^5~\mu\text{m}^3$ at pH = 2.43 to $1.04\times10^6~\mu\text{m}^3$ at pH = 13.95 condition. The evolution of average coefficient of friction (COF), defined as COF = F_f/F_n , where F_f is the frictional force and F_n is the normal force, as a function of sliding time is shown in Fig. 6 (c). It can be seen that the average COF also increased with increasing pH values.

Since the same mechanical load was applied on the same material during tribocorrosion, whose mechanical wear was expected to be constant under all pH conditions, the observed increase of material loss as a function of increasing pH is believed to be dominated by the corrosion properties of the alloy. From the electrochemical measurements, it was shown that this MPEA had the highest dissolution rate in the basic environment, hence its higher material loss during tribocorroison. In addition, the surface roughness of wear track also

increased slightly with increasing pH, from $R_a=0.42\,\mu m$ under acidic to 0.49 μm under basic condition. This result could explain the trend of COF, in which the higher surface roughness led to more contacting asperities, hence higher COF values and fluctuations.

3.4. Post-tribocorrosion characterization via SEM, XPS, and TEM analysis

Fig. 7 shows the surface SEM image and the corresponding EDS maps after tribocorroison tests. Under all pH conditions, higher concentrations of oxygen (O) were detected within the wear track than those in the unworn area, similar to those observed during dry wear [77]. The amount of Cl was more pronounced in the acidic and neutral conditions, which was absent from the wear track under basic condition. At pH = 13.95, it is likely that the more OH $^-$ ions reduces the surface adsorption of Cl $^-$ ions.

Fig. 8(a) summarizes the average composition (at.%) of all elements detected on the worn and unworn surface from EDS analysis. Additional comparison of the passive layer composition after corrosion and tribocorrosion under various pH values can be found in **Table S1** of the Supplemental Materials. The concentrations of all constituting elements of the MPEA change differently in the worn and unworn areas as a function of pH. Under the acidic and neutral conditions, Cr and Fe was depleted while Ni content was higher in the wear track than the unworn areas. It is likely that more dissolution of Co and Fe at the surface during tribocorrosion leaves behind a Ni-rich layer underneath. In the basic solution, only a slight depletion (~ 2.5 at.%) of Cr was observed while all other elements remained almost constant from within and outside the wear track. The differences in chemical composition as a function of pH strongly indicated that the passive layer, although present under

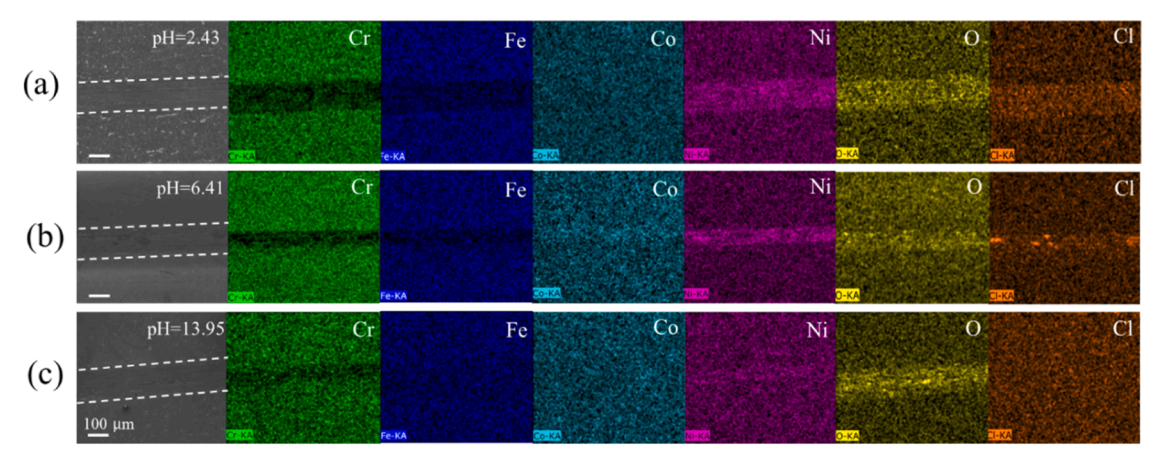


Fig. 7. Surface SEM images and the corresponding EDS elemental mappings of $Al_{0.1}$ CrCoFeNi after tribocorrosion tests under (a) pH=2.43, (b) pH=6.41, and (c) pH=13.95 conditions. Scale bar in all images represents100 μ m.

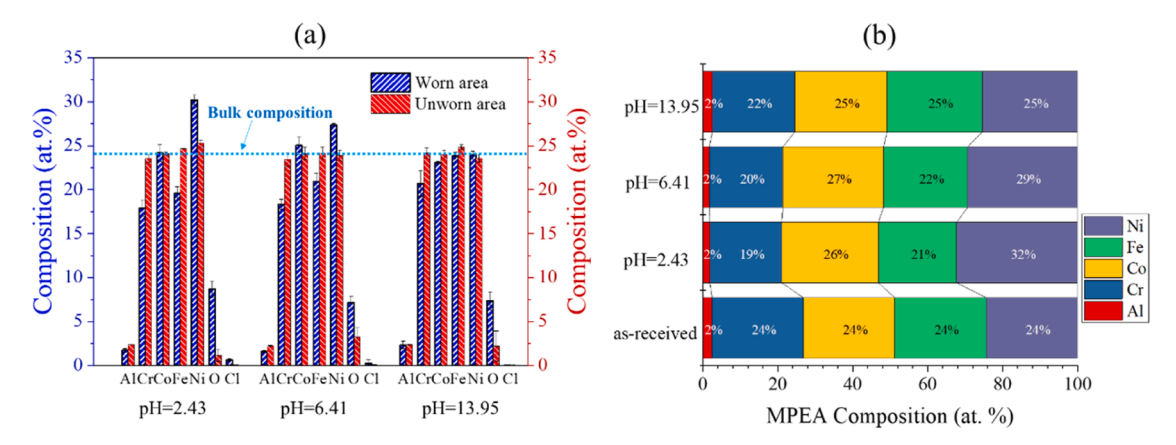


Fig. 8. Elemental composition (at.%) on the (a) worn and unworn areas, and (b) as-received vs. worn area of Al_{0.1}CrCoFeNi after tribocorrosion tests under different pH conditions.

different pH values, were formed mainly from Cr and Ni in the acidic and neutral solutions, and from all principal elements in the basic solution. This is rather surprising given that the thermodynamics of the Cr-H $_2$ O system (as shown by the Pourbaix diagram in Fig. 12), pure Cr is expected to be soluble under acidic conditions, hence not forming a protective oxide layer. Fig. 8(b) compares the composition of the worn area vs. the as-received sample. The worn area composition at pH= 13.95 is quite similar to that of the as-received sample, which shows good repassivation behavior. The worn area composition at pH = 2.41, and 6.41 shows a clear reduction of Cr concentration and increase of Ni concentration as compared to the as-received sample, which leads to their poor repassivation behavior.

To gain a better understanding of surface oxidation state, XPS analysis was carried out from both worn and unworn areas, as summarized in Fig. 9 for Cr and Ni. Due to space limit, a complete list of high resolution XPS spectrums of all other principal elements (Co and Fe) is provided in the Supplementary Materials Fig. S3. In addition, Table S2 provides a summary of XPS binding energy values used in the fittings, percentages of different species found, and possible compounds that could be formed using Cr and Ni as examples. The results show that the passive film on the worn and unworn areas of MPEA at all pH was mainly composed of Cr and Ni oxides, followed by smaller amounts of Co and Fe-based oxides. This is in good agreement with atom probe results from pure corrosion tests and previous reports on corrosion of NiCr alloys [78] and MPEAs with similar compositions [28]. The Ni oxide and hydroxide indexed is NiO and Ni(OH)2, while the Cr oxide and hydroxide is Cr_2O_3 , $Cr(OH)_3$, and likely some Cr^{6+} [78]. The oxide/metal

phase fraction of each element was summarized in Table 2, obtained by calculating the area under the corresponding XPS peak. For simplicity, the oxide phase fraction includes the peaks of all oxides and (if any) hydroxide of each element. It was found that under acidic and neutral pH conditions, the $M_{\rm ox}/X$ ratio in the worn area was always larger than that in unworn area. Under basic pH condition, the $M_{\rm ox}/X$ ratio in the worn area is very similar to that of the unworn area, in good agreement with results in Fig. 8.

Finally, to investigate the subsurface composition and structure, TEM analysis was carried out on the samples tribocorroded at pH=2.43 and 13.95. Fig. 10(a) shows a HAADF-STEM image of the tribocorroded cross-sectional sample from pH=2.43. The corresponding elemental maps for Fe, Ni, Co, Al, Cr, and O are shown in Fig. 10(b). The line profile in Fig. 10(c) corresponds to the red dashed arrow in Fig. 10(a). The dashed white circles in Al and O maps in Fig. 10(b) highlight areas of high Al and O concentration accompanied by the local depletion of the other constituent elements Cr, Co, Ni, and Fe, likely due to the incorporation of wear debris from the counterbody (alumina). The black arrows in Fig. 10(b) and (c) show an increased concentration of Ni right below the worn surface of the alloy with a simultaneous decrease in Cr and Fe. In addition, there exists a thin oxide layer roughly 5 nm thick which corresponds to an increase of Al content and a concentration decrease of other elements, such as Fe, Ni, and Cr. These results indicate that Al₂O₃ is preferentially formed during corrosion despite the nominal Al content being significantly lower than the other constituent elements. Based on these results, the tribocorroded oxide layer, defined as having oxygen concentrations above ~ 10 at.%, has a depth of ~ 110 nm, with

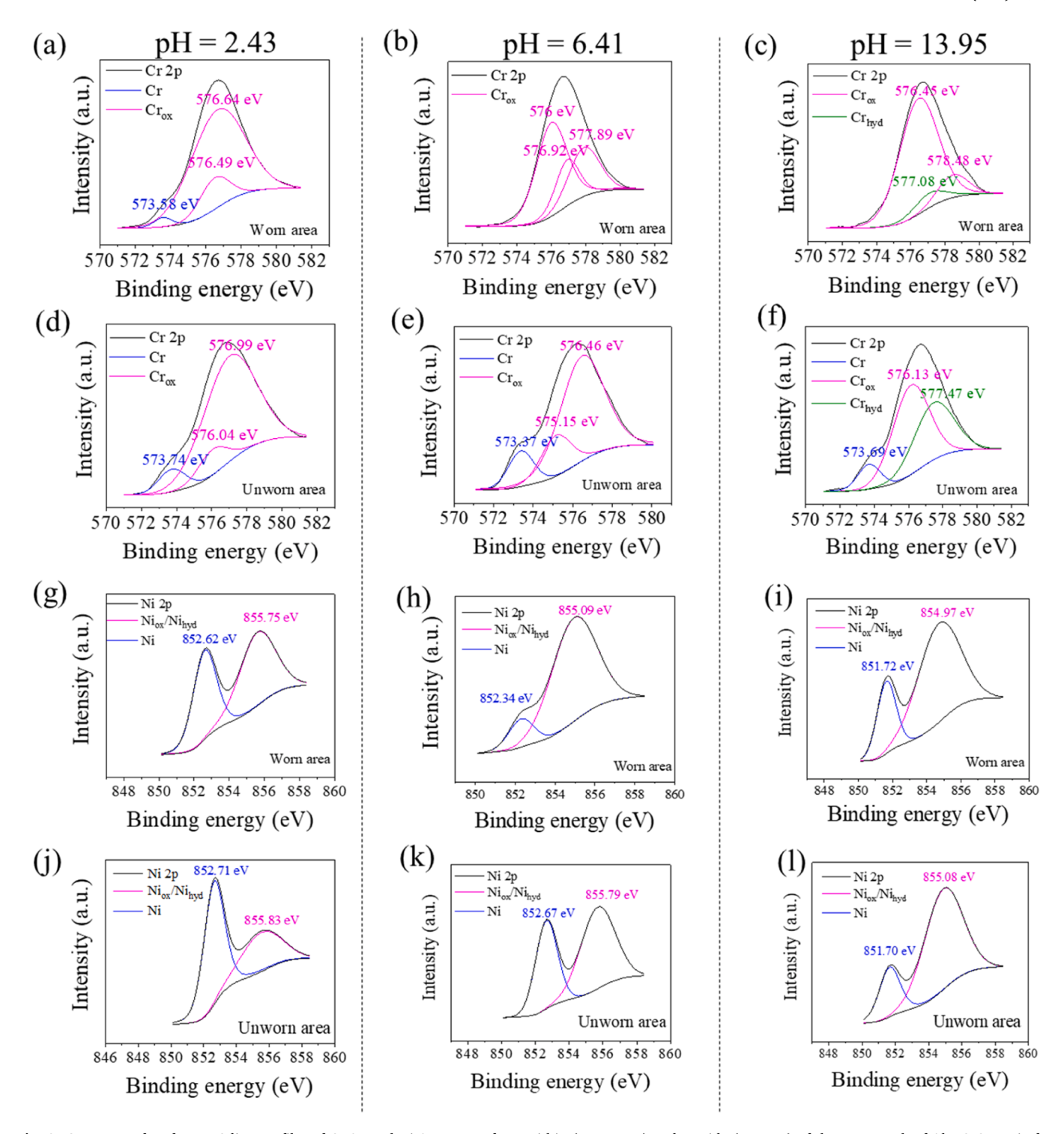


Fig. 9. Summary of surface XPS line profiles of Cr 2p and Ni 2p spectra from within (worn area) and outside (unworn) of the wear track of $Al_{0.1}$ CrCoFeNi after tribocorrosion tests under different pH conditions.

an outermost layer of ~ 30 nm that contains oxides of all principal elements, and a subsurface layer of ~ 80 nm that is Ni-rich.

Fig. 11 shows a HAADF-STEM image of the MPEA tribocorroded at pH=13.95 solution. The oxide layer in this sample is about 170 nm. The depth of this tribocorroded oxide layer is relatively uniform which contrasts to the non-uniform 110-nm layer seen in the pH=2.43 sample. Like the previous sample, areas with the increased Al and O concentrations are detected, as indicated by the dashed white circles in Al and O maps in Fig. 11(b). The black arrow in Fig. 12(c) shows the position of an Al-rich region in the EDS line scan. These regions correspond with an

increase in O content and a decrease in Fe, Ni, Co, and Al. The key difference here is that no Ni-rich layer is detected in the sample tribocorroded in the basic solution.

4. Discussions

4.1. Thermodynamics of surface repassivation

Summarizing all experimental results from the previous section, we show that at the acidic and neutral pH, during either pure corrosion or

Table 2 Summary of the oxide/metal phase fraction in the worn and unworn areas on Al $_{0.1}$ CrCoFeNi after tribocorrosion at various pH conditions, determined from XPS analysis. For simplicity, metal oxide phase fractions of each element (e.g. Cr_{ox} and Ni_{ox}) is calculated by summing all its oxides and (if any) hydroxide peaks.

Solution pH	Oxide/metal phase fraction				
	Worn area		Unworn area		
pH = 2.43	Cr _{ox} /Cr	34.86	Cr _{ox} /Cr	10.35	
	Ni _{ox} /Ni	1.25	Ni _{ox} /Ni	0.56	
	Fe _{ox} /Fe	0.42	Fe _{ox} /Fe	0.69	
	Co _{ox} /Co	1.95	Co _{ox} /Co	1.05	
pH = 6.41	Cr _{ox} /Cr	Cr oxide only	Cr _{ox} /Cr	6.61	
	Ni _{ox} /Ni	6.23	Ni _{ox} /Ni	1.41	
	Fe _{ox} /Fe	2.02	Fe _{ox} /Fe	3.87	
	Co _{ox} /Co	1.31	Co _{ox} /Co	0.81	
pH = 13.95	Cr _{ox} /Cr	10.78	Cr _{ox} /Cr	9.38	
	Ni _{ox} /Ni	3.01	Ni _{ox} /Ni	3.37	
	Fe _{ox} /Fe	1.65	Fe _{ox} /Fe	1.83	
	Co _{ox} /Co	2.41	Co _{ox} /Co	2.04	

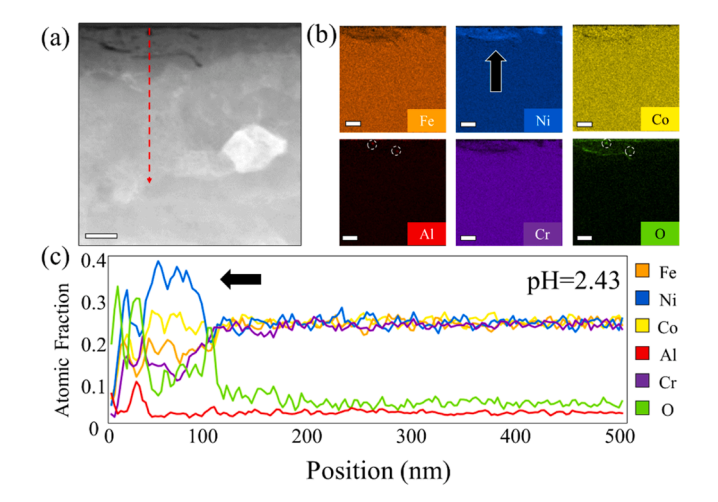


Fig. 10. (a) HAADF-STEM image of tribocorroded sample at pH=2.43. Dashed red arrow indicates EDS line profile direction shown in (c). (b) Corresponding elemental maps of Fe, Ni, Co, Al, Cr, and O respectively. The scale bars in (a–c) all represent 100 nm. (For interpretation of the references to colour in this figure legend, the reader is referred to the web version of this article.)

tribocorrosion, the surface oxide layer contains mostly Cr- and Ni-oxide, with a subsurface Ni-rich layer which is also partially oxidized, and slightly depleted in Cr and Fe. Surfaces with such characteristics eventually result in poor repassivation capability after chemical (i.e. pitting) or mechanical (i.e. wear) removal of the passive film. On the other hand, the surface oxide layer under basic solution contains a higher fraction of Ni-oxide and an absence of any Ni-rich subsurface layer. Such surfaces lead to excellent repassivation capability. It is also noted that the concentration of Cr in this Ni-rich layer is \sim 20 at.% and 22 at.% at the acidic and neutral pH respectively after corrosion, and ~ 19 at.% and 20 at.% at the acidic and neutral pH respectively after tribocorrosion. These values are slightly lower than the bulk composition, but still significantly higher than the $\sim 10\text{-}12$ at % minimum concentration needed to provide surface passivity in NiCr and NiFeCrMnCo MPEAs [28]. Thus, the fact that Ni participates in surface oxidation, rather than being 'left behind' to form a Ni-rich layer below the outermost oxide, is identified to be the key factor for sustained repassivation capability.

To understand the different oxidation behavior at different pH, the thermodynamics of metal surface corrosion can be understood in terms of Pourbaix diagrams [79,80]. Fig. 12 shows the calculated Pourbaix diagram of all major constituting elements (Al, Cr, Co, Fe, and Ni), binary $(Cr_{50}Ni_{50})$, equi-atomic ternary alloy $(Cr_{33}Co_{33}Fe_{33}, Cr_{33}Co_{33}Ni_{33})$

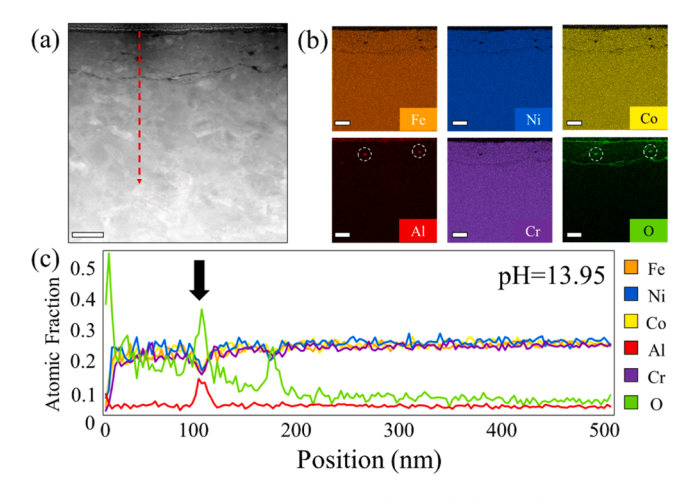


Fig. 11. (a) HAADF-STEM image of tribocorroded sample at pH=13.95. Dashed red arrow indicates the location of the EDS line profile shown in (c). (b) Individual elemental maps of the area scanned in (a) for Fe, Ni, Co, Al, Cr, and O respectively. The scale bars in (a–g) all represent 100 nm. (For interpretation of the references to colour in this figure legend, the reader is referred to the web version of this article.)

 $Co_{33}Fe_{33}Ni_{33}$, and $Fe_{33}Ni_{33}Cr_{33}$), as well as $Al_{0.1}CrCoFeNi$, equiatomic CrCoFeNi, and $Cr_{19}Co_{26}Fe_{21}Ni_{34}$. Due to space limit, more detailed Pourbaix diagrams of the quaternary and quinary alloys are shown in the Supplementary Materials **Figs. S3 and S4**.

The formation of a complex alloy significantly enhanced the passive region than that of the single element metal, mainly due to the formation of Cr-, and Co-oxides at acidic to neutral pH, and Fe- and Ni-oxides and hydroxide at basic pH. From the Pourbaix diagram of the quaternary CrCoFeNi (Fig. 12(k)) and quinary Al_{0.1}CrCoFeNi (Fig. 12(l)) MPEA alloys, it can be seen that this MPEA is corroding in acidic condition and becomes passive in neutral to basic solution due to fact that all principal elements participate in surface oxidation. This is in good agreement with the experimental observations from the previous section. The effects of the addition of small amounts of Al on the corrosion behavior of this MPEA can be understood by comparing the Pourbaix diagrams of Al_{0.1}CrCoFeNi and equiatomic CrCoFeNi. Tables S2 and S3 in the Supplemental Materials summarize the non-soluble solid and soluble ionic phases formed at various pH values of these two compositions. For easy comparison with the experimental results, potentials listed in Tables S3 and S4 are converted to Ag/AgCl. It was found that Al addition did not change the overall corrosion/passivation regions in the diagram. It mainly results in the following differences in the phase formations in $Al_{0.1}$ CrCoFeNi as compared to CrCoFeNi: at pH = 2.43, additional Al³⁺ is formed; at pH=6.41, additional solid phase of Al₂O₃ with a molar fraction of 3.4% is formed; at pH=13.95, additional (AlO₂)⁻ is formed. Due to the passivation ability of Al in neutral pH, it is thus not surprising that Al only participates in surface oxidation at pH=6.41. These results are indeed in agreement with APT results presented in Figs. 3-5, where Al ions are largely absent in the passive layer in the acidic and basic solution, but present in the neutral solution with \sim 2-2.5 at.% in the passive layer.

Note that for Ni, it heavily participated in surface oxidation at pH=13.95 by forming NiFe₂O₄(38.3% molar fraction) and NiO(10.5% molar fraction) phases with relatively high molar fraction among all oxides (Table S3). The whole oxide composition includes: $\text{Co}_3\text{O}_4(12.8\%)$, $\text{CoCr}_2\text{O}_4(38.3\%)$, NiFe₂O₄(38.3%), and NiO(10.5%). All principal elements (Cr, Co, Ni, Fe) participate in surface oxidation under such conditions. On the other hand, in acid to neutral solutions, the surface oxides mainly include $\text{CoCr}_2\text{O}_4(48.3\%)$, $\text{CoFe}_2\text{O}_4(34.4\%)$, and a small amount of NiFe₂O₄(13.9%). In other words, Ni is largely absent in the surface oxides, and its subsequent dissolution in the electrolyte could be impeded by the presence of the surface oxide layer, resulting in its

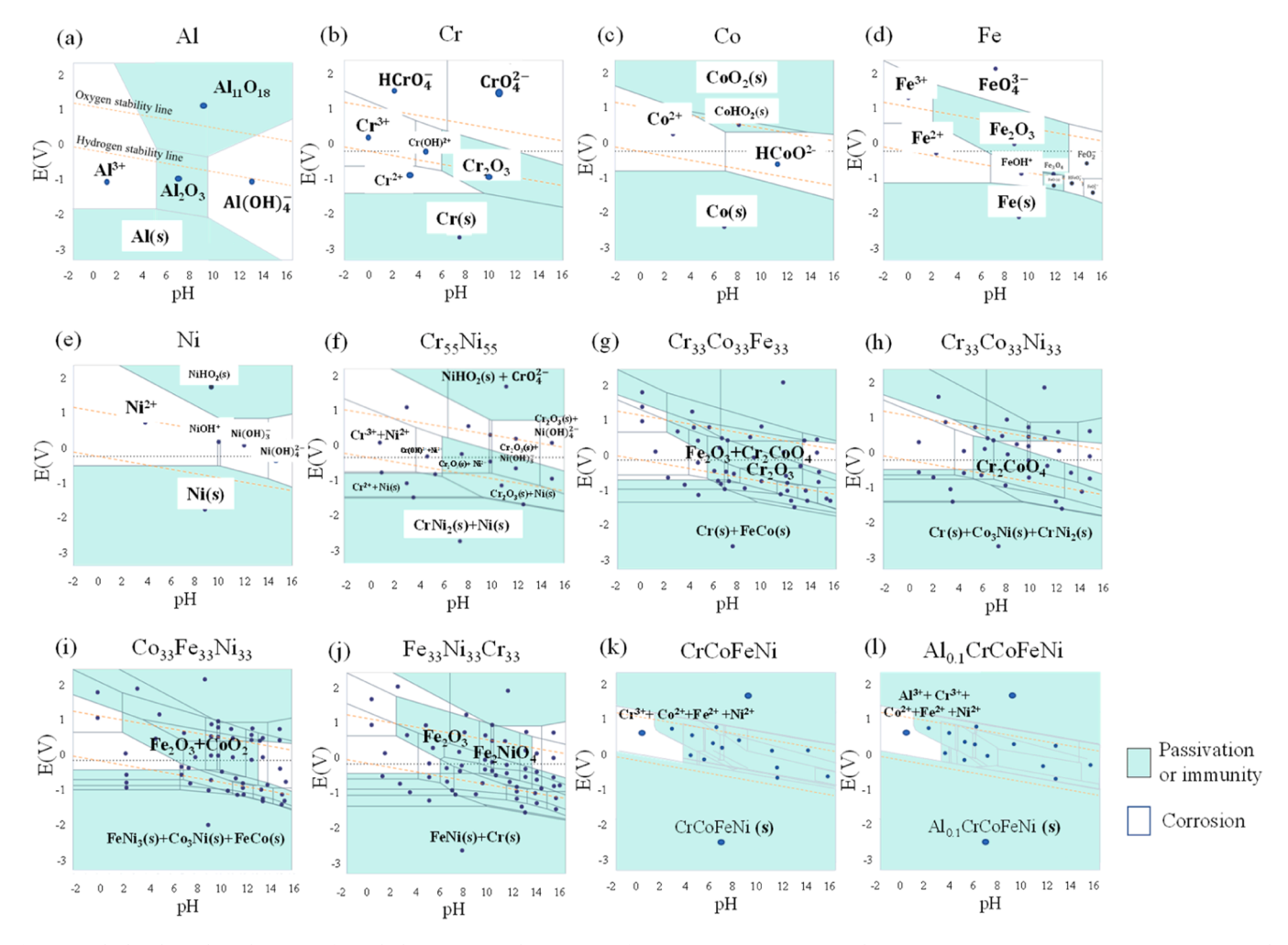


Fig. 12. Calculated Pourbaix diagrams of (a) Al. (b) Cr, (c) Co, (d) Fe, (e) Ni, (f) $Cr_{55}Ni_{55}$, (g) $Cr_{33}Co_{33}Fe_{33}$, (h) $Cr_{33}Co_{33}Ni_{33}$, (i) $Co_{33}Fe_{33}Ni_{33}$, (j) $Fe_{33}Ni_{33}Cr_{33}$, (k) $Cr_{05}ENi_{13}$, and (l) $Al_{0.1}Cr_{05}ENi_{13}$. Potential (E) is plotted against standard hydrogen potential in all diagrams.

enrichment at the substrate/oxide interface. Such altered subsurface composition would no longer be equiatomic, but rather enriched in Ni. Fig. S4 (b, c) shows a comparison of Pourbaix diagram of equiatomic CrCoFeNi vs. a Ni-enriched composition ($Cr_{19}Co_{26}Fe_{21}Ni_{34}$), the latter of which is based on the experimental results of worn surface composition at pH=2.43 (Fig. 8(b)). Negligible difference is observed from such diagrams since shapes of the Pourbaix diagram are largely determined by the number of alloy elements and is not sensitive to compositional change. However, the Ni-enrichment in $Cr_{19}Co_{26}Fe_{21}Ni_{34}$ alloy also results in a reduction of Cr concentration, from \sim 24.5 at.% to 19 at.%. As shown in Fig. 12(i, k), the passive region becomes significantly smaller and corrosion potential is lower when Cr is removed from the composition, largely in agreement with our main conclusions.

Interestingly, based on the calculated Pourbaix diagram, at pH = 2.43 and around -0.3 to 0.2 V vs. Ag/AgCl (Figs. 12(l) and S4(a)), corrosion, rather than passivation, is expected to occur in this MPEA system since no oxide formation is expected. However, the presence of a passive layer is confirmed by both the electrochemical and tribocorrosion tests. These results suggest that in MPEA system, it is possible to form metastable oxide phases in the acidic environment, contradictory to the thermodynamic predictions, which is key to the passivity of MEPA under both corrosion and tribocorrosion conditions. More work is needed in the future to systematically understand the atomic structure and formation mechanisms of these metastable phases.

4.2. Insights on the effects of alloy composition on the repassivation kinetics from DFT calculations

To understand the lack repassivation capability in the pH=2.43 case. we used its surface composition experimentally measured (from Fig. 8 (b)), which is Cr₂₅Co₃₄Fe₂₇Ni₄₄, to construct a unit cell in DFT. Comparatively, an equiatomic Cr25Co25Fe25Ni25 unit cell was used to represent the tribocorroded surface composition at pH=13.95, similar to our previous work [7]. Fig. 13(a) represents the unit cell of these two surface compositions. A lattice constant of 3.54 Å was obtained for both Cr₁₉Co₂₆Fe₂₁Ni₃₄ and Cr₂₅Co₂₅Fe₂₅Ni₂₅. To understand the repassivation process from the view of surface chemical stability, the electron work function (EWF) was calculated to help explain the difference of OCP evolution between pH=2.43 and pH=13.95. EWF is the minimum energy required to extract an electron from a solid at Fermi level to vacuum. Results in Fig. 13(c) reveal that the (111) surface exhibits the highest EWF, while the (110) surface presents the lowest EWF for both compositions. The EWF for the pH=2.43 composition is 4.272 eV, significantly higher than that observed for the pH=13.95 case (4.173 eV). Higher EWF often indicates a slower oxidation tendency and repassivation rate [81,82], which could help explain the slow OCP recovery at pH=2.43. Table S5 in the Supplemental Materials summarizes the EWF of CoCrFeNi-based MPEAs from prior DFT and/or experimental studies. Our calculated results in Fig. 13(c) are in general agreement with these prior studies. In addition, Table S5 shows that both alloying composition (e.g. in Al_xCoCrFeNi) and crystallographic orientation (e.g. (111) vs. (110) plane of CoCrFeNi) affect EWF in a similar trend as

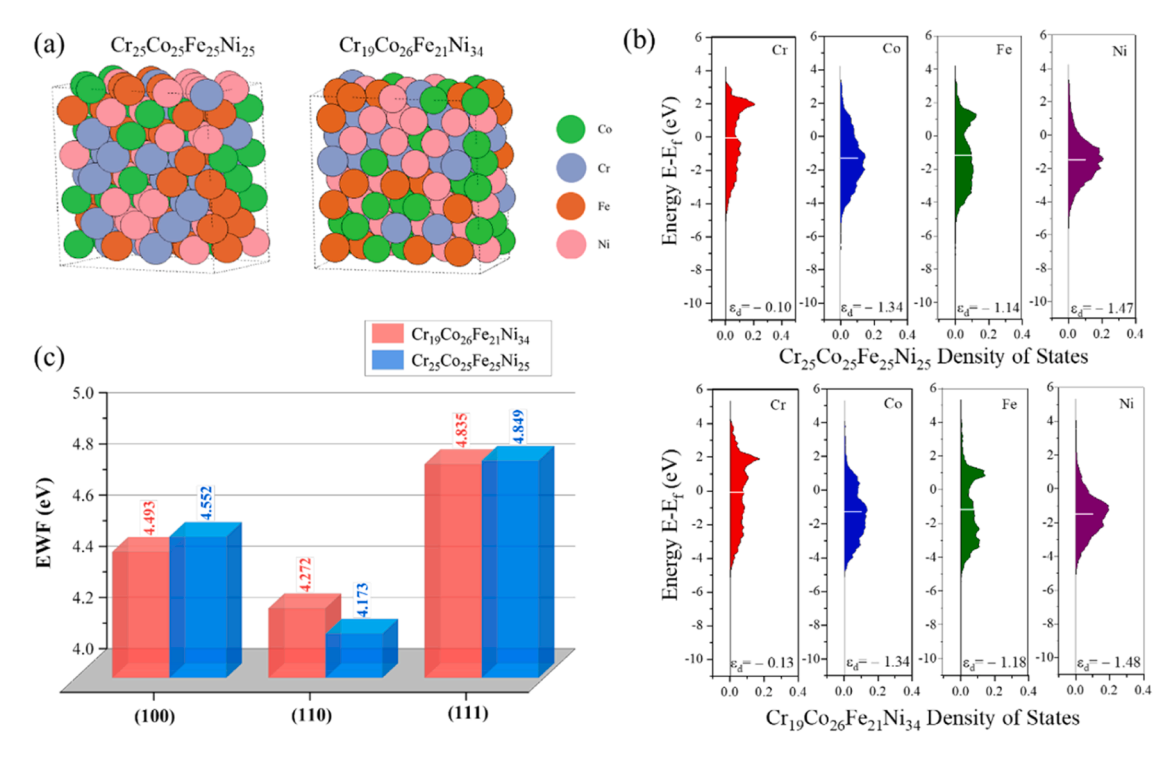


Fig. 13. DFT calculation results. (a) Unit cell from SQS, (b) PDOS of Cr, Co, Fe and Ni elements on (110) surfaces, and (c) electron work function of equiatomic $(Cr_{25}Co_{25}Fe_{25}Ni_{25})$ and Ni-rich $(Cr_{19}Co_{26}Fe_{21}Ni_{34})$ CrCoFeNi MPEAs.

predicted by our results. The Projected Density of States (PDOS) for both alloy compositions are illustrated in Fig. 13(b). The d-band center of Co, Fe and Ni do not exhibit significant differences between the two alloy compositions. However, a noticeable shift in the d-band center of Cr from -0.10 eV in the pH=13.95 case to -0.13 eV in the pH=2.43 case is observed. This shift away from the Fermi level indicates a decrease in chemical reactivity for Cr, which may also contribute to the slow OCP recovery in the pH=2.43 case.

4.3. A simple repassivation model for CrCoFeNi MPEA

Finally, Fig. 14 schematically summarizes a simple repassivation model for CrCoFeNi MPEAs based on results of this work. First of all, corrosion of MPEA leads to different surface composition as a function of pH due to the different corrosion/passive behavior of individual

principal elements. While traditional alloy design such as stainless steel focus on one or two passive elements such as Cr and Ti, MPEA design is more challenging due to the complex roles of four or more element with high concentrations (typically >10 at.%). In the CrCoFeNi alloy system, the corroded surface at pH of ~ 2.4 - 6.8 contains a Cr- and Ni-rich passive layer, followed by a Ni-enriched subsurface layer as a result of selective dissolution of Fe and Co. Such composition modification due to surface reaction directly affects the subsequent repassivation when the passive film is damaged chemically via pitting or mechanically via tribocorrosion. As shown in the first row of Fig. 14, the corroded surface composition at pH <7 is significantly different from the bulk composition. Once the passive film is damaged, this new surface cannot fully repassivate to the initial state. On the other hand, at the basic conditions, all principal elements participate in the surface oxidation and there is an absent of the Ni-rich layer. As a result, the repassivation ability of MPEA

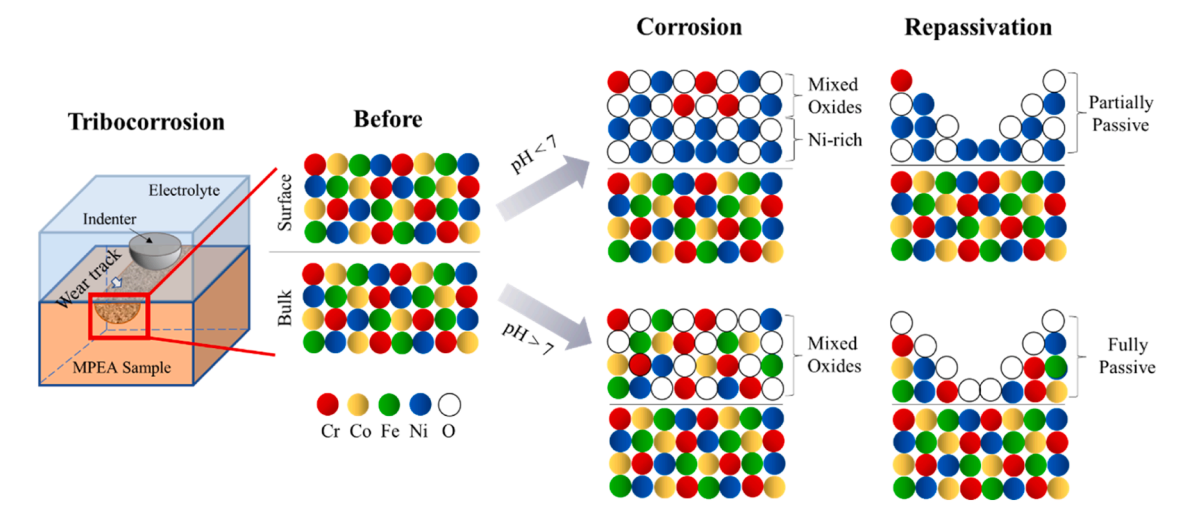


Fig. 14. Schematic illustration representing the surface and subsurface composition and the associated tribocorrosion mechanisms of CrCoFeNi MPEA as a function of pH.

is fully restored.

We note that the formation of a Ni-rich layer due to corrosion here resembles the dealloying effect observed in Fe-Ni-based alloys to some extent [83,84]. For example, Ghaznavi et al. [83] showed that in Fe-Ni and Fe-(Cr)-Ni alloys, the preferential dissolution of the less-noble metals (LN), i.e. Fe, from a homogenous fcc solid solution resulting in a porous layer enriched in the more-noble metal(s), i.e. Ni. The dealloying parting limit, i.e. the atom fraction of the LN element below which dealloying does not occur, is related to the availability of a continuous path of LN element atoms through the metal lattice, also known as site percolation. For fcc systems, percolation dealloying implies a dealloying threshold of 20 at% of LN elements, which is very close to the concentrations of the principal element in equiatomic MPEAs. A similar concentration limit of Cr has been found via the percolation theory for alloy passivation by Xie et al. [85] in Fe-Cr and Ni-Cr systems. Thus when designing new MPEAs, it is critical to ensure adequate amounts of more-noble and more passive element are present at all pH conditions. Finally, while this work identifies that lower pH impairs the repassivation ability of MPEA, it is worth noting that such pH-dependent corrosion behavior could potentially be remedied via appropriate alloying in the future. For example, Lutton et al. [86] showed that the addition of 6 at.% Mo to Ni-22Cr alloy could remove its pH sensitivity on passivation. More work is needed in the future to select principal elements and design their compositions to achieve extended passivity and repassivation capability over a wide pH range.

Finally, it is worth noting that the existence of a large body of literature in the field of passivation and corrosion of stainless steel [87–89] is vital for providing context to the current research in MPEAs. For example, the passive film structure of corroded stainless steel shares lots of similarity with MPEAs. Rovere et al. [88] shows that the passive films on stainless steel in H₂SO₄ solutions exhibit a bilayer composition, comprising a highly hydrated outer layer composed of Fe oxyhydroxides and an anhydrous inner layer consisting of Fe-Cr mixed oxides with a spinel structure. It is noteworthy that this spinel contains a significant amount of Cr, as Fe tends to concentrate primarily near the outer oxide surface. Haupt and Strehblow [89] studied the passive layer structure of Fe-15Cr in H₂SO₄ solution and found that in addition to form a bilayer oxide structure of Fe₃O₄/Fe₂O₃, Cr is enriched to \sim 30% at the metal/oxide interface, as compared to 15% in the bulk in the potential range of 0.3-1 V vs. SHE (standard hydrogen electrode). More importantly, they found that Cr accumulates mostly in the first 15 min in the inner part of the layer, and the maximum Cr concentration moves towards the surface with increasing passivation time. If the observed Ni enrichment in the Al_{0.1}CrCoFeNi MPEA follows a growth kinetics pattern akin to that of the Fe-Cr alloy, investigating the repassivation behavior of anodized MPEA after varying anodization times would be one valuable future research direction to understand the synergy between corrosion and surface stress. Another important area of future research in MPEA is to develop an experimentally validated computational modeling framework to simulate the atomic structure and compositional patterning of the passive layer, which has ultimate importance in controlling passivation and repassivation kinetics. Computational tools, such as phase field modeling and reactive force field molecular dynamics simulations, could facilitate the achievement of these objectives.

4. Conclusions

In summary, the effects of pH were found to play an important role on the repassivation behaviors of Al_{0.1}CrCoFeNi MPEAs in 0.6 M NaCl solution. Combining results from the corrosion and tribocorrosion tests, surface characterization via APT, XPS, and TEM, and DFT calculations, the following conclusions can be drawn:

 Al_{0.1}CrCoFeNi MPEAs exhibited passivity in all pH studied and best repassivation capability at pH=13.95 in 0.6 M NaCl solution.

- (2) Acidic to neutral electrolyte and longer scratching time was found to exacerbate the repassivation capability of Al_{0.1}CrCoFeNi MPEAs.
- (3) The selective oxidation of Cr, Co, and Fe in the acidic to neutral solution led to a Ni-rich layer at the oxide/metal interface, which hinders future repassivation.
- (4) DFT studies show that the Ni-rich MPEA composition formed at the acidic condition has higher electron work function than that of the equiatomic composition. In addition, change of d-band center of Cr indicates a reduced chemical reactivity in the acidic solution. All together leads to and slower oxidation tendency and repassivation rate, which could help explain the slow OCP recovery.

Declaration of Competing Interest

The authors declare that they have no known competing financial interests or personal relationships that could have appeared to influence the work reported in this paper.

Acknowledgement

This research was financially supported by the US National Science Foundation (Grant No. DMR-2104655/2104656). APT research was supported by the Center for Nanophase Materials Sciences (CNMS), which is a US Department of Energy, Office of Science User Facility at Oak Ridge National Laboratory. The authors would like to thank James Burns for assistance in performing APT sample preparation and running the APT experiments. This work was performed in part at the Nanoscale Characterization and Fabrication Laboratory, which is supported by the Virginia Tech National Center for Earth and Environmental Nanotechnology Infrastructure (NanoEarth), a member of the National Nanotechnology Coordinated Infrastructure (NNCI), supported by NSF (ECCS 1542100 and ECCS 2025151). J.C. and W.C. gratefully acknowledge the discussion of XPS analysis and results with Dr. Weinan Leng of the Nanoscale Characterization and Fabrication Laboratory at Virginia Tech

Supplementary materials

Supplementary material associated with this article can be found, in the online version, at doi:10.1016/j.actamat.2023.119490.

References

- A. Manzoni, et al., Phase separation in equiatomic AlCoCrFeNi high-entropy alloy, Ultramicroscopy 132 (2013) 212–215.
- [2] J.W. Yeh, et al., Nanostructured high-entropy alloys with multiple principal elements: novel alloy design concepts and outcomes, Adv. Eng. Mater. 6 (5) (2004) 299–303.
- [3] B. Cantor, et al., Microstructural development in equiatomic multicomponent alloys, Mater. Sci. Eng. A Struct. Mater. Prop. Microstruct. Process. 375 (2004) 213–218.
- [4] C.C. Tung, et al., On the elemental effect of AlCoCrCuFeNi high-entropy alloy system, Mater. Lett. 61 (1) (2007) 1–5.
- [5] C.M. Lin, H.L. Tsai, Evolution of microstructure, hardness, and corrosion properties of high-entropy Al0.5CoCrFeNi alloy, Intermetallics 19 (3) (2011) 288–294.
- [6] C.J. Tong, et al., Microstructure characterization of AlxCoCrCuFeNi high-entropy alloy system with multiprincipal elements, Metall. Mater. Trans. A Phys. Metall. Mater. Sci. 36 (4) (2005) 881–893. a.
- [7] Z.Y. Zhang, et al., Computational design of non-equiatomic CoCrFeNi alloys towards optimized mechanical and surface properties, J. Mater. Res. 37 (17) (2022) 2738–2748.
- [8] M.A. Hemphill, et al., Fatigue behavior of Al0.5CoCrCuFeNi high entropy alloys, Acta Mater. 60 (16) (2012) 5723–5734.
- [9] Z. Tang, et al., Fatigue behavior of a wrought Al0.5CoCrCuFeNi two-phase highentropy alloy, Acta Mater. 99 (2015) 247–258.
- [10] W.P. Li, et al., Elevated fatigue crack growth resistance of Mo alloyed CoCrFeNi high entropy alloys, Eng. Fract. Mech. 218 (2019) 1–9.
- [11] J.M. Wu, et al., Adhesive wear behavior of AlxCoCrCuFeNi high-entropy alloys as a function of aluminum content, Wear 261 (5-6) (2006) 513–519.

- [12] M.G. Poletti, et al., Development of a new high entropy alloy for wear resistance: FeCoCrNiW0.3 and FeCoCrNiW0.3+5 at.% of C, Mater. Des. 115 (2017) 247–254.
- [13] A. Poulia, et al., Dry-sliding wear response of MoTaWNbV high entropy alloy, Adv. Eng. Mater. 19 (2) (2017) 1–10.
- [14] N.D. Stepanov, et al., High temperature deformation behavior and dynamic recrystallization in CoCrFeNiMn high entropy alloy, Mater. Sci. Eng. A Struct. Mater. Prop. Microstruct. Process. 636 (2015) 188–195.
- [15] N. Kumar, et al., Understanding effect of 3.5 wt.% NaCl on the corrosion of Al0.1CoCrFeNi high-entropy alloy, J. Nucl. Mater. 495 (2017) 154–163.
- [16] Y.Z. Shi, et al., Homogenization of AlxCoCrFeNi high-entropy alloys with improved corrosion resistance, Corros. Sci. 133 (2018) 120–131.
- [17] Y.Y. Chen, et al., Electrochemical kinetics of the high entropy alloys in aqueous environments - a comparison with type 304 stainless steel, Corros. Sci. 47 (11) (2005) 2679–2699.
- [18] A.A. Jalbuena, et al., Corrosion of Al0.1CoCrFeNi high entropy alloy in a molten eutectic salt, J. Electrochem. Soc. 166 (11) (2019) C3488–C3492.
- [19] Y.J. Hsu, W.C. Chiang, J.K. Wu, Corrosion behavior of FeCoNiCrCux high-entropy alloys in 3.5% sodium chloride solution, Mater. Chem. Phys. 92 (1) (2005) 112–117
- [20] P. Schmutz, G.S. Frankel, Characterization of AA2024-T3 by scanning Kelvin probe force microscopy, J. Electrochem. Soc. 145 (7) (1998) 2285–2295.
- [21] L.A. de Oliveira, R.M.P. da Silva, R.A. Antunes, Scanning Electrochemical Microscopy (SECM) study of the electrochemical behavior of anodized AZ31B magnesium alloy in simulated body fluid, Mater. Res. Ibero-Am. J. Mater. 22 (5) (2019) 1–8.
- [22] X. Chen, et al., Emergence of micro-galvanic corrosion in plastically deformed austenitic stainless steels, Mater. Des. 203 (2021) 1–9.
- [23] S. Shuang, et al., Corrosion resistant nanostructured eutectic high entropy alloy, Corros. Sci. 164 (2020) 1–14.
- [24] P.P. Ding, et al., Preparation, characterization and properties of multicomponent A1CoCrFeNi(2.1) powder by gas atomization method, J. Alloys Compd. 721 (2017) 609–614.
- [25] N. Birbilis, et al., A perspective on corrosion of multi-principal element alloys, npj Mater. Degrad. 5 (1) (2021) 14.
- [26] F.G. Coury, G. Zepon, C. Bolfarini, Multi-principal element alloys from the CrCoNi family: outlook and perspectives, J. Mater. Res. Technol. 15 (2021) 3461–3480.
- [27] Z. Zhang, et al., Computational design of non-equiatomic CoCrFeNi alloys towards optimized mechanical and surface properties, J. Mater. Res. 37 (17) (2022) 2738–2748.
- [28] A.Y. Gerard, et al., The role of chromium content in aqueous passivation of a non-equiatomic Ni38Fe20CrxMn21-0.5xCo21-0.5x multi-principal element alloy (x = 22, 14, 10, 6 at%) in acidic chloride solution, Acta Mater. 245 (2023), 118607.
- [29] S.B. Inman, et al., Corrosion behavior of a compositionally complex alloy utilizing simultaneous Al, Cr, and Ti passivation, Corros. Sci. 217 (2023), 111138.
- [30] Z. Wang, et al., Repassivation and dry sliding wear behavior of equiatomic medium entropy TiZr (Hf, Ta, Nb) alloys, Mater. Lett. 312 (2022), 131643.
- [31] I.U. Toor, Repassivation kinetics and its role in SCC prediction-a review, Int. J. Electrochem. Sci. 9 (6) (2014) 2737–2755.
- [32] H. Mraied, W.J. Cai, The effects of Mn concentration on the tribocorrosion resistance of Al-Mn alloys, Wear (2017) 191–202. 380-381.
- [33] J. Chen, W.J. Cai, Effect of scratching frequency on the tribocorrosion resistance of Al-Mn amorphous thin films, Wear 426 (2019) 1457–1465.
- [34] K.W. Wang, et al., Understanding tribocorrosion of aluminum at the crystal level, Acta Mater. 245 (2023).
- [35] K.W. Wang, et al., Multiphysics modeling and uncertainty quantification of tribocorrosion in aluminum alloys, Corros. Sci. 178 (2021).
- [36] K.W. Wang, W.J. Cai, Modeling the effects of individual layer thickness and orientation on the tribocorrosion behavior of Al/Cu nanostructured metallic multilayers, Wear 477 (2021) 1–11.
- [37] Z. Tun, J.J. Noël, D.W. Shoesmith, Electrochemical modification of the passive oxide layer on a Ti film observed by in situ neutron reflectometry, J. Electrochem. Soc. 146 (3) (1999) 988.
- [38] G.T. Burstein, A.J. Davenport, The current-time relationship during anodic oxide film growth under high electric field, J. Electrochem. Soc. 136 (4) (1989) 936.
- [39] D.D. Macdonald, The point defect model for the passive state, J. Electrochem. Soc. 139 (12) (1992) 3434.
- [40] M. Brocklebank, et al., Mechanism of titanium electrochemical oxidation via isotopic labeling, high resolution ion depth profiling, and impedance spectroscopy, Electrochim. Acta 435 (2022), 141342.
- [41] G.T. Burstein, P.I. Marshall, Growth of passivating films on scratched 304l stainless-steel in alkaline-solution, Corros. Sci. 23 (2) (1983) 125–137.
- [42] M. Barbosa, J.C. Scully, The role of repassivation kinetics in the measurement of the pitting potential of AISI-304 stainless-steel by the scratch method, Corros. Sci. 22 (11) (1982) 1025, p.-&.
- [43] R. Bandy, R. Roberge, D. Vanrooyen, Intergranular failures of alloy-600 in high-temperature caustic environments, Corrosion 41 (3) (1985) 142–150.
- [44] H.S. Kwon, E.A. Cho, K. Yeom, Prediction of stress corrosion cracking susceptibility of stainless steels based on repassivation kinetics, Corrosion 56 (1) (2000) 32–40.
- [45] E.A. Cho, et al., Quantitative analysis of repassivation kinetics of ferritic stainless steels based on the high field ion conduction model, Electrochim. Acta 45 (12) (2000) 1933–1942.
- [46] B. Deng, et al., Critical pitting and repassivation temperatures for duplex stainless steel in chloride solutions, Electrochim. Acta 53 (16) (2008) 5220–5225.
- [47] N. Yang, et al., Corrosion and tribocorrosion mitigation of perhydropolysilazanederived coatings on low carbon steel, Corros. Sci. 177 (2020) 1–11.

[48] W.B. Wang, et al., Ultrahigh tribocorrosion resistance of metals enabled by nanolayering, Acta Mater 206 (2021) 1–12.

- [49] W.B. Wang, et al., Effects of nanosecond laser shock peening on residual stress, corrosion and tribocorrosion behavior of WE43 magnesium alloys, Wear 524 (2023) 1–8.
- [50] W.B. Wang, et al., Enabling high-performance surfaces of biodegradable magnesium alloys via femtosecond laser shock peening with ultralow pulse energy, ACS Appl. Bio Mater. 4 (11) (2021) 7903–7912.
- [51] A. Ayyagari, et al., Reciprocating sliding wear behavior of high entropy alloys in dry and marine environments, Mater. Chem. Phys. 210 (2018) 162–169.
- [52] R.B. Nair, et al., High entropy alloys: prospective materials for tribo-corrosion applications, Adv. Eng. Mater. 20 (6) (2018) 1–9.
- [53] K. Kuwabara, et al., Mechanical and corrosion properties of AlCoCrFeNi highentropy alloy fabricated with selective electron beam melting, Addit. Manuf. 23 (2018) 264–271.
- [54] Y.F. Kao, et al., Electrochemical passive properties of AlxCoCrFeNi (x=0, 0.25, 0.50, 1.00) alloys in sulfuric acids, Corros. Sci. 52 (3) (2010) 1026–1034.
- [55] Z. Wang, et al., Effect of pH on the electrochemical behaviour and passive film composition of 316L stainless steel, Acta Metall. Sin. Engl. Lett. 32 (5) (2019) 585–598
- [56] L. Freire, et al., The passive behaviour of AISI 316 in alkaline media and the effect of pH: a combined electrochemical and analytical study, Electrochim. Acta 55 (21) (2010) 6174–6181.
- [57] K. Thompson, et al., In situ site-specific specimen preparation for atom probe tomography, Ultramicroscopy 107 (2-3) (2007) 131–139.
- [58] A.M. Patel, et al., Efficient Pourbaix diagrams of many-element compounds, Phys. Chem. Chem. Phys. 21 (45) (2019) 25323–25327.
- [59] A.K. Singh, et al., Electrochemical Stability of Metastable Materials, Chem. Mater. 29 (23) (2017) 10159–10167.
- [60] K.A. Persson, et al., Prediction of solid-aqueous equilibria: scheme to combine first-principles calculations of solids with experimental aqueous states, Phys. Rev. B Condens. Matter Mater. Phys. 85 (23) (2012) 1–12.
- [61] G. Kresse, J. Furthmüller, Efficient iterative schemes for ab initio total-energy calculations using a plane-wave basis set, Phys. Rev. B 54 (16) (1996) 11169–11186.
- [62] G. Kresse, D. Joubert, From ultrasoft pseudopotentials to the projector augmentedwave method, Phys. Rev. B 59 (3) (1999) 1758–1775.
- [63] J.P. Perdew, K. Burke, M. Ernzerhof, Generalized Gradient Approximation Made Simple, Phys. Rev. Lett. 77 (18) (1996) 3865–3868.
- [64] A. Zunger, et al., Special quasirandom structures, Phys. Rev. Lett. 65 (3) (1990) 353–356.
- [65] A. van de Walle, et al., Efficient stochastic generation of special quasirandom structures. Calphad 42 (2013) 13–18.
- [66] R.B. Nair, et al., Exceptionally high cavitation erosion and corrosion resistance of a high entropy alloy, Ultrason. Sonochem. 41 (2018) 252–260.
- [67] S. Guo, et al., Effect of valence electron concentration on stability of fcc or bcc phase in high entropy alloys, J. Appl. Phys. 109 (10) (2011) 1–5.
- [68] L. Lei, et al., A comparative study on the critical pitting criteria of a super ferritic stainless steel at different temperatures in chloride or bromide solution, Corros. Sci. 183 (2021), 109311.
- [69] Y.T. Sun, et al., A comparative study on potentiodynamic and potentiostatic critical pitting temperature of austenitic stainless steels, Mater. Corros. 69 (1) (2018) 44–52.
- [70] R. Silva, et al., A comprehensive study of the pitting corrosion mechanism of lean duplex stainless steel grade 2404 aged at 475°C, Corros. Sci. 191 (2021), 109738.
- [71] S. Choudhary, et al., Recent insights in corrosion science from atomic spectroelectrochemistry, Electrochem. Sci. Adv. 2 (6) (2022), e2100196.
- [72] X. Li, et al., Spontaneous passivation of the CoCrFeMnNi high entropy alloy in sulfuric acid solution: the effects of alloyed nitrogen and dissolved oxygen, Corros. Sci. 196 (2022), 110016.
- [73] J.D. Henderson, et al., Molybdenum surface enrichment and release during transpassive dissolution of Ni-based alloys, Corros. Sci. 147 (2019) 32–40.
- [74] Z. Wang, et al., Investigation of the deterioration of passive films in H2S-containing solutions, Int. J. Miner. Metall. Mater. 24 (8) (2017) 943–953.
- [75] A. Lopez-Ortega, J.L. Arana, R. Bayon, Tribocorrosion of passive materials: a review on test procedures and standards, Int. J. Corros. 2018 (2018), 7345346.
- [76] J.L. Gilbert, S.A. Mali, Y. Liu, Area-dependent impedance-based voltage shifts during tribocorrosion of Ti-6Al-4V biomaterials: theory and experiment, Surf. Topogr. Metrol. Prop. 4 (3) (2016), 034002.
- [77] J.P. Celis, P. Ponthiaux, F. Wenger, Tribo-corrosion of materials: interplay between chemical, electrochemical, and mechanical reactivity of surfaces, Wear 261 (9) (2006) 939–946.
- [78] B.P. Payne, M.C. Biesinger, N.S. McIntyre, Use of oxygen/nickel ratios in the XPS characterisation of oxide phases on nickel metal and nickel alloy surfaces, J. Electron Spectrosc. Relat. Phenom. 185 (5) (2012) 159–166.
- [79] K. Wang, et al., Potential-pH diagrams considering complex oxide solution phases for understanding aqueous corrosion of multi-principal element alloys, npj Mater. Degrad. 4 (1) (2020) 35.
- [80] B. Zhang, Y. Zhang, S.M. Guo, A thermodynamic study of corrosion behaviors for CoCrFeNi-based high-entropy alloys, J. Mater. Sci. 53 (20) (2018) 14729–14738.
- [81] Z. Wang, et al., Wettability, electron work function and corrosion behavior of CoCrFeMnNi high entropy alloy films, Surf. Coat. Technol. 400 (2020), 126222.
- [82] Y. Luo, et al., Electron work function: an indicative parameter towards a novel material design methodology, Sci. Rep. 11 (1) (2021) 11565.
- [83] T. Ghaznavi, et al., Alloying effects in high temperature molten salt corrosion, Corros. Sci. 197 (2022), 110003.

- [84] T. Ghaznavi, S.Y. Persaud, R.C. Newman, The effect of temperature on dealloying mechanisms in molten salt corrosion, J. Electrochem. Soc. 169 (11) (2022),
- [85] Y. Xie, et al., A percolation theory for designing corrosion-resistant alloys, Nat. Mater. 20 (2021) 1-5.
- [86] K. Lutton, et al., Passivation of Ni-Cr and Ni-Cr-Mo alloys in low and high pH sulfate solutions, J. Electrochem. Soc. 170 (2) (2023), 021507.
- [87] C.O.A. Olsson, D. Landolt, Passive films on stainless steels—chemistry, structure and growth, Electrochim. Acta 48 (9) (2003) 1093–1104.

 [88] C.A. Della Rovere, et al., Characterization of passive films on shape memory
- stainless steels, Corros. Sci. 57 (2012) 154-161.
- [89] S. Haupt, H.H. Strehblow, A combined surface analytical and electrochemical study of the formation of passive layers on FeCr alloys in 0.5 M H₂SO₄, Corros. Sci. 37 (1) (1995) 43-54.